Spring 2013

Biomechanical implications of congenitally bicuspid aortic valves: a finite element analysis of patient-specific geometry

Paul Nicholas Jermihov
University of Iowa

BIOMECHANICAL IMPLICATIONS OF CONGENITALLY BICUSPID AORTIC VALVES: A FINITE ELEMENT ANALYSIS OF PATIENT-SPECIFIC GEOMETRY

by

Paul Nicholas Jermihov

An Abstract

Of a thesis submitted in partial fulfillment of the requirements for the Doctor of Philosophy degree in Biomedical Engineering in the Graduate College of The University of Iowa

May 2013

Thesis Supervisors: Professor Krishnan B. Chandran
Associate Professor Jia Lu

This thesis introduces a framework aimed at developing an aid for physicians to diagnose and manage failing aortic valves using finite element (FE) simulations. The bicuspid aortic valve (BAV) is the most commonly observed valvular defect (Sievers et al. 2007) and therefore used to investigate the clinical utility of FE-based mechanical simulations. For the analysis, patient data was collected using real-time 3D echocardiography (rt3DE) of five normal valves and three pathological. The valve geometries were reconstructed into 3D models including the sinus and leaflet structures. An FE analysis was completed on the models, and the results were critically analyzed and validated with experimental data. Results indicate that human patient aortic valves can be successfully reconstructed and when simulated, realistic deformation is observed. This thesis focused on severity assessment of BAV morphologies through comparison to that of normal aortic valves.

Abstract Approved: _____

Thesis Supervisor

_____

Title and Department

_____

Date

_____

Thesis Supervisor

_____

Title and Department

_____

Date

BIOMECHNICAL IMPLICATIONS OF CONGENITALLY BICUSPID AORTIC VALVES: A FINITE ELEMENT ANALYSIS OF PATIENT-SPECIFIC GEOMETRY

by

Paul Nicholas Jermihov

A thesis submitted in partial fulfillment of the requirements for the Doctor of Philosophy in Biomedical Engineering in the Graduate College The University of Iowa

May 2013

Thesis Supervisors: Professor Krishnan B. Chandran
Associate Professor Jia Lu

Graduate College The
University of Iowa Iowa City,
Iowa

CERTIFICATE OF APPROVAL

PH.D. THESIS

This is to certify that the Ph. D. thesis

Paul Nicholas Jermihov

has been approved by the Examining Committee for the thesis requirement for the Doctor of Philosophy degree in Biomedical Engineering at the May 2013 graduation.

Thesis Committee:

Krishnan B. Chandran, Thesis Supervisor

Jia Lu, Thesis Supervisor

Madhavan L. Raghavan

Sarah Vigmostad

Nicole M. Grosland

TABLE OF CONTENTS

LIST OF TABLES iii

LIST OF FIGURES iv

CHAPTER ONE: INTRODUCTION 1

1.1 Background 1
1.2 Motivation 8
1.3 Specific Aims 8

CHAPTER TWO: ANATOMY AND PHYSIOLOGY 10

2.1 Tri-Leaflet Valve 10
2.2 Bicuspid Valve 10
2.3 Valvular and Ascending Aortic Complications 12

CHAPTER THREE: GEOMETRY CONSTRUCTION 13

3.1 Motivation 13
3.2 Model Geometries 13
3.3 Geometrical validation 19

CHAPTER FOUR: MECHANICAL ANALYSIS FORMULATION 22

4.1 Continuum Mechanics 22
4.1.1 Finite Deformation of Solids 22
4.1.2 Stress and Strain Definition 23
4.2 Balance Equations 24
4.3 Finite Element Formulation 25
4.4 Explicit vs. Implicit Solution Method 26

CHAPTER FIVE: FE ANALYSIS 29

5.1 Material Properties 29
5.2 Boundary Condition 34
5.3 Results 37
5.3.1 Opening Phase 41
5.3.2 Closing Phase 43

CHAPTER SIX: DISCUSSION AND CONCLUSION 49

6.1 Significance of the study 49
6.2 Limitations 55

6.3 Future Work 56

REFERENCES 67

APPENDIX 62

LIST OF TABLES

Table

1. GEOMETRIC AREAS OF THE LEAFLETS FOR EACH VALVE..... 18

2. MEASUREMENTS (MM) USED TO VALIDATE RELEVANT DIMENSIONS OF PATIENT TAV1..... 19

3. MEASUREMENTS (MM) USED TO VALIDATE RELEVANT DIMENSIONS OF PATIENT BAV1..... 20

4. PERCENT INCREASE OF BAV STRESS FROM SIMILAR AVERAGED TAV VALUES..... 48

LIST OF FIGURES

FIGURE

1. ILLUSTRATION OF NORMAL TAV (TOP) AND PATHOLOGICAL BAV..... 1

2. CARPENTIER-EDWARDS PERIMOUNT BHV..... 3

3. IDEALIZED GEOMETRIES OF THE NORMAL AORTIC VALVE (LEFT MOST) AND THREE PATHOLOGICAL BAV..... 7

4. TO CAPTURE THE CONTACT AREA FROM THE PATIENT IMAGED DATA IN EACH OF THE CONTACTING LEAFLETS THE SINGLE SURFACE PROVIDED WAS DUPLICATED BY ROTATE ABOUT THE AXIS MADE BY THE COMMISSURE..... 15

5. LEAFLET AND SINUS VIEWS OF TAV1..... 16

6. LEAFLET AND SINUS VIEWS OF BAV1. THE NONCORONARY AND RIGHT LEAFLET FORM THE CONJOINT CUSP IN THIS PATIENT..... 17

7. TO COMPARE THE COMPLETED GEOMETRY AND THE INITIAL PATIENT POINT CLOUD DATA THE TWO ARE SHOWN SUPERIMPOSED ON ONE ANOTHER..... 21

8. FIBER DIRECTIONS ASSIGNED TO THE LEAFLETS..... 30

9. ILLUSTRATION OF SKIN APPLICATION USED FOR MASS PROPORTIONAL DAMPING COEFFICIENT IMPLEMENTATION TO ACCOUNT FOR THE VISCOUS FORCE DISSIPATION BY THE BLOOD..... 33

10. ILLUSTRATION OF APPLIED BOUNDARY CONDITIONS..... 35

11. THE TIME-VARYING PRESSURE LOAD APPLIED TO THE LEAFLETS AND ROOT STRUCTURES..... 36

12. ALL GEOMETRIES WERE MESHED USING TRIANGULAR SHELL ELEMENTS ON NODES GENERATED WITH A SPACING OF 0.8 NODES PER MILLIMETER..... 37

13. THE VALVE BEGINS IN THE FULLY CLOSED POSITION FROM THE PRECEDING CYCLE (END DIASTOLE)..... 38

14. TRANSVALVULAR PRESSURE BEGINS TO OPEN THE VALVE..... 39

15. THE VALVE IS APPROXIMATELY HALF WAY OPEN..... 39

16. AT THIS POINTS, 0.14 SECONDS INTO THE CURRENT SIMULATION THE VALVES REACH THE FULLY OPEN CONFIGURATION (MID SYSTOLE)..... 40

17. ILLUSTRATION OF EOA AND GOA OUTLINED IN RED AND GREEN RESPECTIVELY..... 40

18. PLANAR EXTRACTION OF EOA OF EACH VALVE IN THE FULLY OPEN CONFIGURATION..... 41

19. TOP DOWN PERSPECTIVE OF EACH VALVE IN THE FULLY OPEN CONFIGURATION..... 43

20. ILLUSTRATION SHOWING LEAFLET COAPTATION AT TIME OF FULL CLOSURE..... 44

21. RESULTS SHOWING THE COMPUTED MAXIMUM OF AMOUNT OF COAPTATION VERSUS THE AREA EXTRACTED FROM THE IMAGED DATA..... 45

22. MAXIMUM IN-PLANE PRINCIPAL STRESS CONTOURS..... 46

23. MAXIMUM IN-PLANE STRESS OF BAV(1-3) COMPARED TO THE TAV AVERAGE..... 47

24. SIDE BY SIDE COMPARISON OF TAV5 (LEFT) AND BAV2 (RIGHT)..... 50

25. FULL OPEN ORIFICE OF TAV AND BAV COMPARED WITH THE FE PREDICTED RESULTS (LEFT COLUMN) AND ECHO IMAGE OF THE SAME VALVE (RIGHT COLUMN)..... 51

26. SMALLEST LEAFLET TO TOTAL VALVULAR SURFACE AREA RATIO SHOWN IN COMPARISON TO AVERAGED PATIENT SPECIFIC VALUES (DOTTED LINE) AND IDEALIZED FRACTION (SOLID LINE)..... 53

27. PLOT OF PEAK IN PLANE PRINCIPAL STRESS AGAINST LEAFLET AREA RATIO..... 53

A1. COMPLETED ANNULUS AND LEAFLET STRUCTURE..... 66

A2. LEAFLET ATTACHMENT BOUNDARY IDENTIFIED FOR TAV..... 67

A3. CIRCULAR PLANES GENERATED FOR ANNULUS AND SINUS CONSTRUCTION..... 69

A4. SINUS GENERATION FROM POINT CLOUD DATA..... 71

CHAPTER ONE: INTRODUCTION

1.1 Background

Recent innovations with computational methods provide new tools for physicians to continue simulation-based medical planning [1-2]. Current understanding of anatomical and physiological disease pathology is limited to physician-reported data, which varies greatly from patient to patient. As computational costs decrease and computational methods improve in accuracy, the use of computational simulations becomes a more viable route in developing treatment strategies for individual patients [3-4]. This thesis introduces a framework for the analysis of individual patient-specific aortic valves, more specifically, the morphological variants engendered by the presence of a congenitally bicuspid aortic valve (BAV), shown in Figure 1.

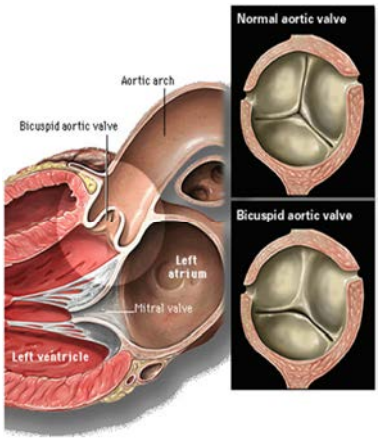

Figure 1. Illustration of normal TAV (top) and pathological BAV. The BAV pictured shows the most common variant, fusion of the left and right leaflets.

BAV is prevalent in 1%–2% of the population, making it the most prominent congenital heart valve defect [5]. Generally, BAV occurs twice as often in males, but in families with more than one occurrence of a BAV, no gender bias exists [6]. BAV is often associated with other vascular complications, including aortic regurgitation (AR), infective endocarditis (IE), coarcation of the aorta (COA), aortic dissection, and ascending aortic dilation [5]. Nearly 33% of all patients with a BAV will experience major cardiac complications and will require surgical intervention during their lifetime [5]. BAV is the most prevalent heart valve defect and carries the highest risk of morbidity and mortality [5-8]. It was first identified as a pathological anomaly by Paget in 1844 and associated with severe calcific stenosis by Peacock in 1866 [9]. Osler, in 1886, identified the likelihood of infective endocarditis with the presence of a BAV [9].

In the biomedical field, FE analysis techniques have been implemented for the identification of stress pattern distribution and mechanics of the aortic valve, the purpose being to elucidate failure mechanisms and also aid in replacement heart valve development. The aortic valve is a good candidate for FE analysis due to its inaccessible location and complex function. Grande et al. published a FE study of the aortic valve in the end diastole configuration based on MRI patient data of nine subjects. The resulting study pointed out asymmetries inherent in the valve as well as in the orifices for the left and right coronary arteries [9-10]. Gnyaneshwar et al. presented a dynamic analysis of an aortic root and leaflet complex, beginning in the mid-systole configuration for a full cardiac cycle simulation [11]. Kim et al. employed a valve geometry similar to that of a typical bioprosthetic heart valve (BHV), shown in

Figure 2, and presented a dynamic FE analysis of the BHV aimed at investigating sources of calcification and tissue degeneration [12-14].

Figure 2. Carpentier-Edwards perimount BHV.

Recently, Conti et al. have developed a model of the normal aortic valve, and in a later publication a similar technique was employed to generate a BAV model. Valve dimensions were obtained through averaging dimensions extracted from patient MRI data. This process was extended to eight normotensive patients with functioning bicuspid aortic valves [15-16]. To further expand on the study of BAV, the analysis presented in this thesis employs eight individual patient-specific geometries, five normal TAV and three BAV.

Previous studies have conducted simulations of aortic valves with the intent of investigating causes of valvular failure and improving future prosthetic valve designs [11-14, 17-26]. A few studies relevant to the trileaflet analysis section of this thesis include computational and experimental normal aortic valve studies and bicuspid aortic valves. Gnyaneshwar et al. (2002), De Hart et al. (2003), Sun et al. (2005), and Kim et al. (2007) have conducted computational simulations of normal aortic heart valves comparable to the trileaflet simulations conducted in this thesis. Gnyaneshwar et al. (2002) conducted a dynamic simulation of the entire cardiac cycle using ABAQUS/Explicit, employing an isotropic linear material model. The objective of the study was to investigate the effect of leaflet and aortic root interaction on valve function. The analysis employed shell elements, linear elastic material properties, and proper contact controls, and it simulated the entire cardiac cycle. The aortic root had an elastic modulus twice that of the valve leaflet, 2 MPa. It was found that expansion of the aortic root is most important during the beginning of systole. The maximum von Mises stresses during opening and closing were 30kPa and 800kPa, respectively. These maxima were located in the leaflet attachment regions, which is clinically relevant because those regions are commonly associated with tearing, calcification, and valvular failure [11]. De Hart et al. (2003) conducted a fluid structure interaction (FSI) analysis on an aortic valve. The material model employed was isotropic Neo-Hookean. The FSI analysis provides leaflet mechanical and blood flow data, including their interactions. The maximum von Mises stresses computed during the cardiac cycle were 12kPa and 60kPa in the opening and closing phases, respectively. However, due to limitations of the FSI capabilities, the maximum Reynolds number was 900, which is much less than the 4500 expected physiologically [20].

Much of the current study is built upon research from Michael Sack's group at the University of Pittsburgh and Hyunggun Kim at the University of Iowa. Sacks et al. and Kim et al., have reported on the experimental measurements of Fung material model constants for in-plane deformation of bioprosthetic aortic valve tissue as well as geometrical characterization of BHV from Edward Lifesciences [12-14, 17-18, 23-25, 27]. Sacks et al. reported on a quasi-static FE analysis of the BHV valve closure employing the experimentally measured material properties for the valve leaflet. Kim et al. (2007) extended the study by conducting a dynamic simulation of the full cardiac cycle, including a non-coupled bending model experimentally derived to describe the flexural response. It was found that the major in-plane principal strains during full closure agreed well with the corresponding results from experimental results from Sun et al. (2005) [12-14, 18, 27]. Based on the previously mentioned studies, Jermihov et al. conducted a TAV simulation employing geometry similar to that of Kim et al., the primary difference being the use of a Fung material model derived from fresh porcine aortic valve tissue versus glutaraldehyde-treated bovine pericardium. Peak stress during the simulated valve closure was computed to be 202 kPa [28]. This simulation was then extended to the idealized BAV geometries. It was found that the stresses and strains of TAV are more sensitive to alterations in geometry such as BAV than they are to varied material parameters. More specifically, it was found that the geometry that most closely modeled the most common morphology of BAV (Type IV in Jermihov et al.) had the largest sensitivity to stress increase with material variation than did the other geometries. The other simulated BAV geometries yielded stress sensitivities closer to that of the normal TAV. In a more patient-specific analysis, Conti et al. employed patient MRI data from 10 healthy human subjects to create a model of the aortic

valve root and leaflet structures. To increase the realism of the finite element analysis, a transversely isotropic and incompressible hyperelastic material model was employed for the leaflets. The root structures were assigned linear material properties of 2 MPa and 1MPa for the sinus and interleaflet triangles, respectively. A time-varying uniform pressure was applied to the leaflets and sinus structures equal to the difference between normal aortic and ventricular pressures during the human cardiac cycle. The reported peak in-plane principal stress was 759 kPa [15].

Robicsek et al. (2004) conducted an experimental analysis of BAV geometries along with a computational fluid dynamic (CFD) analysis [29]. The experimental setup consisted of three silicone molds of various BAVs excised from human cadavers. One of the molds tested was similar to that of the BAV geometry in the current study, possessing a raphe and fusion of two leaflets. The CFD analysis of that study employed the mid-systole geometry of the BAV mentioned into an aortic root and aorta domain. The resulting hemodynamics was evaluated. Grande et al. published a finite element study focusing on asymmetrical effects of the root and leaflet geometry of normal aortic valves. Using data from 9 healthy subjects, a single aortic root model was made that maintained the asymmetries of the valve in vivo as much as possible. The constitutive material models employed in this study were of the linear type, with Young's modulus of 334 kPa and 6885 kPa for the leaflets and root, respectively. Thickness of the tissues was assigned physiologically similar values taken from literature. It was found that peak stress values were located in the noncoronary leaflet and lowest in the left leaflet, 538 kPa and 410 kPa, respectively. Investigating the pathological condition of BAV, Weinberg et al. proposed a multiscale model for BAV and TAV. The BAV model was similar to the TAV model,

but leaflets of two equal sizes were generated along with three length scales, organ-tissue-cellular [30]. Jermihov et al. created geometrically idealized models of the most commonly observed BAV morphologies and conducted a corresponding finite element analysis [28]. The resulting idealized geometries are shown in Figure 3. Conti el al. have also published results and FE simulation of BAV. The geometry of the BAV model was constructed from 2D MRI data of 8 normotensive patients. This study yielded a peak in-plane principal stress of 2.9 MPa. In an FE analysis of idealized BAV geometry, Jermihov et al. found a maximum in-plane principal stress of 519 kPa [28].

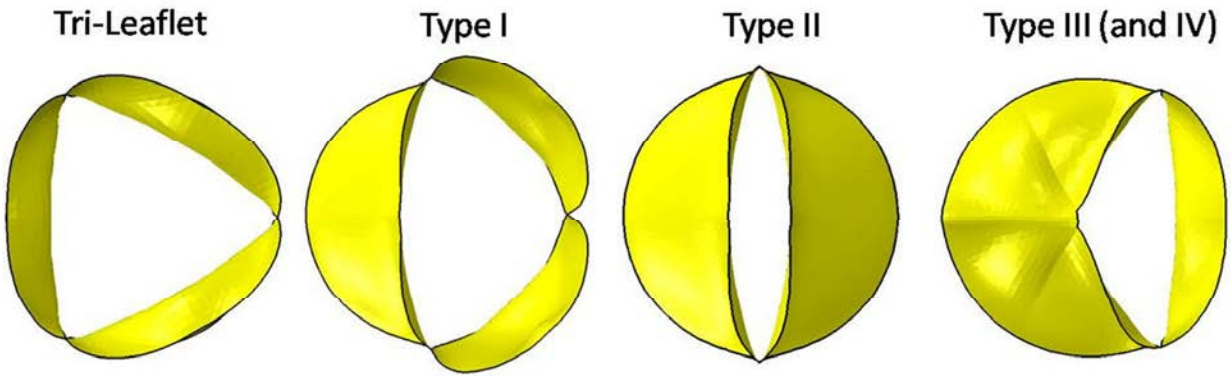

Figure 3. Idealized geometries of the normal aortic valve (leftmost) and three pathological BAV.

1.2 Motivation

In vivo and ex vivo experimentation to quantify the mechanical effects of BAV has been limited; treatment strategy development for BAV is challenging, because the morphology of the valves can vary greatly [6-10, 29, 31-33]. Current studies have assessed symptomatic leaflet geometries associated with higher risks of failure, but there have been relatively few investigations into the mechanical effects of unique root-leaflet BAV geometry [16, 29-30]. This study, employing patient-specific TAV and BAV geometry, is aimed at further understanding failure mechanisms present in the BAV that engender early failure. The long-term goal of such an analysis is to determine the ability of mechanical analysis of BAV to stratify patients who may be at risk of developing valvular pathology as an aid for better patient management by physicians.

1.3 Specific Aims

This analysis aims to utilize real-time 3-D echocardiography (rt3DE) of patient-specific data to create geometries of trileaflet (TAV) and bicuspid aortic valves (BAV), including the root, with non-uniform rational B-splines (NURBS), and then generate a finite element mesh. Employing NURBS as a basis for the geometry is useful for implementation in isogeometric-based finite element solvers because it simplifies the contact resolution and is better able to accurately capture the smooth continuous geometry of the valve structures [3-4]. The second aim is to conduct a dynamic FE analysis of the patient geometries in order to critically compare TAV and BAV dynamics and identify a potential relationship between leaflet stress and valve pathology.

Challenges associated with this FE analysis include NURBS surface generation, leaflet contact, anisotropic tissue properties, short duration of the cardiac cycle, complex patient geometry, and large deformations. The FE analysis software package used was ABAQUS/Explicit because of its efficacy in solving dynamic contact problems involving large deformations.

CHAPTER TWO: ANATOMY AND PHYSIOLOGY

2.1 Tri-Leaflet Valve

During systole, the aortic valve allows blood to flow from the left ventricle to the aorta and prevents backflow during diastole. It is a passive structure that consists of three leaflets or semilunar cusps attached to a connective tissue sleeve or aortic root, which is secured to a fibrous ring [1]. Normal aortic valve tissue is composed of three layers: fibrosa, spongiosa, and ventricularis [1]. The fibrosa, on the aortic side of the leaflet, provides a thick, fibrous scaffold [1]. The central layer of the leaflet is the spongiosa, consisting of loose connective tissue, proteins, and glycosaminoglycans (GAGs) [1]. The ventricularis, similar to the fibrosa but relatively thin, adds another fibrous layer composed of collagen and elastin on the ventricular side of the leaflet [1]. The collagen cords are aligned so that the preferred fiber direction of the valve tissue is circumferential [1]. The radius of the leaflets is larger than the radius of the valve ring, creating a region of coaptation during closure; this region of overlap is important in evaluating healthy valve function and is known as the lunula [1]. The lunula aids in sealing the valve shut, preventing regurgitation [1].

2.2 Bicuspid Valve

BAV is an aortic valve pathology in which the leaflets are malformed during valvular genesis, resulting in leaflet geometry different from that of the normal trileaflet valve [6-7, 34]. The most prevalent form of a BAV is fusion of the left and right valve cusps with a single raphe at the site of fusion [31]. A common feature of the BAV is raphe. The raphe is a tissue mass that forms on the leaflet surface originating at the cusp base. It is not native valve tissue but a thin and fibrous tissue. Raphe exists in several different morphologies, ranging from fractions

to the entire length of the fusion. Calcium deposition often initiates on or near the raphe itself [6, 8, 29, 35-36]. The molecular process of calcium deposition in the BAV is known to be analogous to that of the tricuspid valve [6, 8]. This prevalent BAV form effectively reduces the number of leaflets by one, hence bicuspid. In practice, fusion of cusps and presence of raphe is difficult to identify, because they exist in various morphologies, some of which arise from non-congenital conditions. Often it is even difficult to differentiate between a congenitally bicuspid valve and one that has become bicuspid [31]. Bicuspid valve symptoms may occur in a trileaflet valve from severe calcification, endocarditis, or other diseases [32]. Various valve morphologies have been documented and labeled as congenitally bicuspid, ranging from two evenly sized leaflets to a five-cusp valve, albeit infrequently [31]. This study is concerned with the most common form of BAV. A normal trileaflet valve and a malformed BAV are pictured in Figure 1.

Major health risks associated with BAV have changed over the course of time. As effective treatments for rheumatic fever became more prevalent, there was been a decline in mortality associated with post-inflammatory aortic stenosis [32]. Increased life span has made progressive valve degeneration, such as calcification, more prevalent [37]. Accompanying this degenerative calcification is severe stenosis, which occurs in patients 50–60 years of age with BAV versus 70–80 years of age with a normal trileaflet aortic valve [29]. Stenosis essentially reduces the effective orifice area, EOA. The effective orifice area is a planar area that encompasses the peak valvular constricted area. This area alone cannot be used to compare valves well, but in combination with the area of the channel pre-valve or geometric orifice area, GOA, the contraction coefficient can be calculated [38].

2.3 Valvular and Ascending Aortic Complications

The cause of BAV development is unknown, but it has been attributed to deficiencies of microfibrillar proteins and a reduction in fibrillin-1 production during valvular genesis [5]. A reduction of fibrillin-1 in the aortic tissue triggers MMP production that degrades the medial matrix components of the valvular tissue commonly seen in BAV patients [5]. This degradation coincides with complications associated with BAV, including aortic dilation, aneurysms, and aortic dissection [5].

Stenosis is inherent in BAVs; the unequally sized cusps open to form an oval-type shape compared to the trileaflet valve that opens to a circular shape. Half of all adults with severe aortic stenosis have a BAV [6, 31, 35, 39]. Calcification that occurs in the elderly population is degenerative and will eventually lead to stenosis. Patients with a BAV will experience this calcification more rapidly, endangering the patient with severe aortic valve stenosis at an earlier age [6-7, 35]. A study of 374 patients undergoing aortic valve replacement for aortic stenosis reported 46% having a BAV; 35% of those patients had infective endocarditis, and 10% showed signs of degenerative calcification [32].

CHAPTER THREE: GEOMETRY CONSTRUCTION

3.1 Motivation

Finite element analysis coupled with engineering and design began as early as the 1950s and 1960s with its first major applications in the field of aerospace engineering [4]. Although geometry is at the core of finite element analysis, refinement in geometry definition did not emerge until the 1970s and 1980s. Separate from work being done in the FE field, deemed computer-aided engineering (CAE), computational modeling or computer-aided design (CAD) began to develop into its own industry. Current studies have shown that even small changes in geometry can have a large impact on mechanics. For a standard FE analysis, one needs to discretize the desired geometry into several elements. Any change in geometry will require a revised mesh. It is estimated that about 80% of computational analysis time is devoted to mesh generation across the board of applications [4]. With respect to the biomedical engineering field, CAD and CAE have been evolving rapidly. Generally, biological tissue possesses smooth undulating geometry composed of highly elastic fibers and low compressibility [1]. Recreation of these smooth geometries provides added difficulty with mesh generation, as well as analysis difficulties due to the difference between the mesh and the underlying geometry. Some recent studies have begun employing sophisticated geometry construction techniques for FE applications, from patient heart valve diagnostic tools to the design of replacement valves such as the bioprosthetic heart valve (BHV) .

3.2 Model Geometries

Model geometries were constructed using the commercial software package Rhino3D (v4.0 SR8 Seattle, WA) in combination with PointCloud (SYNCODE v1.0). The data has been

segmented into primary valve structures: sinus, individual leaflets, contact area and annulus. It is critical for the imaged data to accurately capture the contact area between each of the leaflets such that the digitally reconstructed leaflets are appropriately dimensioned. Using the contact surface data, two additional separate surfaces are generated by copying the surface +/- five degrees using the commissural height as the axis of rotation. An example of this is shown in Figure 4. Along with the leaflet and annulus data, the contact areas are integrated into the leaflets using NURBS surfaces patches. To create the sinus, two parallel planes defined just above the sino tubular junction (STJ) and just below the annulus are created; these define the location of the top and bottom of the model. They then act as the planes encompassing the end points of the NURBS surfaces constructed with the corresponding patient data set. This process was repeated for five TAV and three BAV models. A more detailed description of how the valve geometry was created can be found in the Appendix. The resulting trileaflet geometries TAV1, TAV2, TAV3, TAV4, and TAV5 are shown in Figure 5. The bicuspid geometries BAV1, BAV2, and BAV3 are shown in Figure 6. The color code adopted for quickly identifying sinus location is as follows: gold = left coronary; green = right coronary; and purple = noncoronary leaflets. In the BAV models the color is the same for the non-conjoint cusp, but the fused leaflet is shown in blue. Geometric surface areas corresponding to the leaflets of each valve are summarized in Table 1.

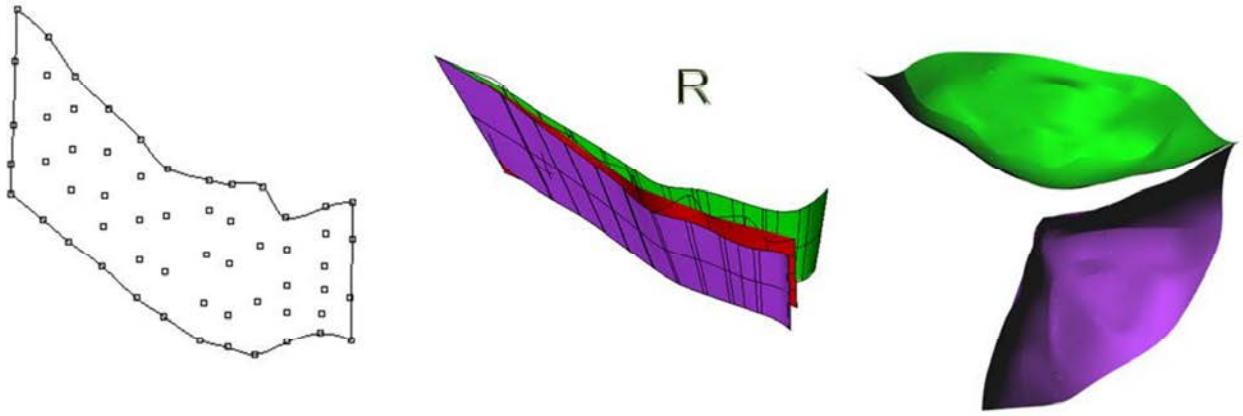

Figure 4. To capture the contact area from the patient imaged data in each of the contacting leaflets the single surface provided was duplicated by a rotation about the axis made by the commissure. The newly created contact surfaces are integrated to the bellies of the corresponding leaflets.

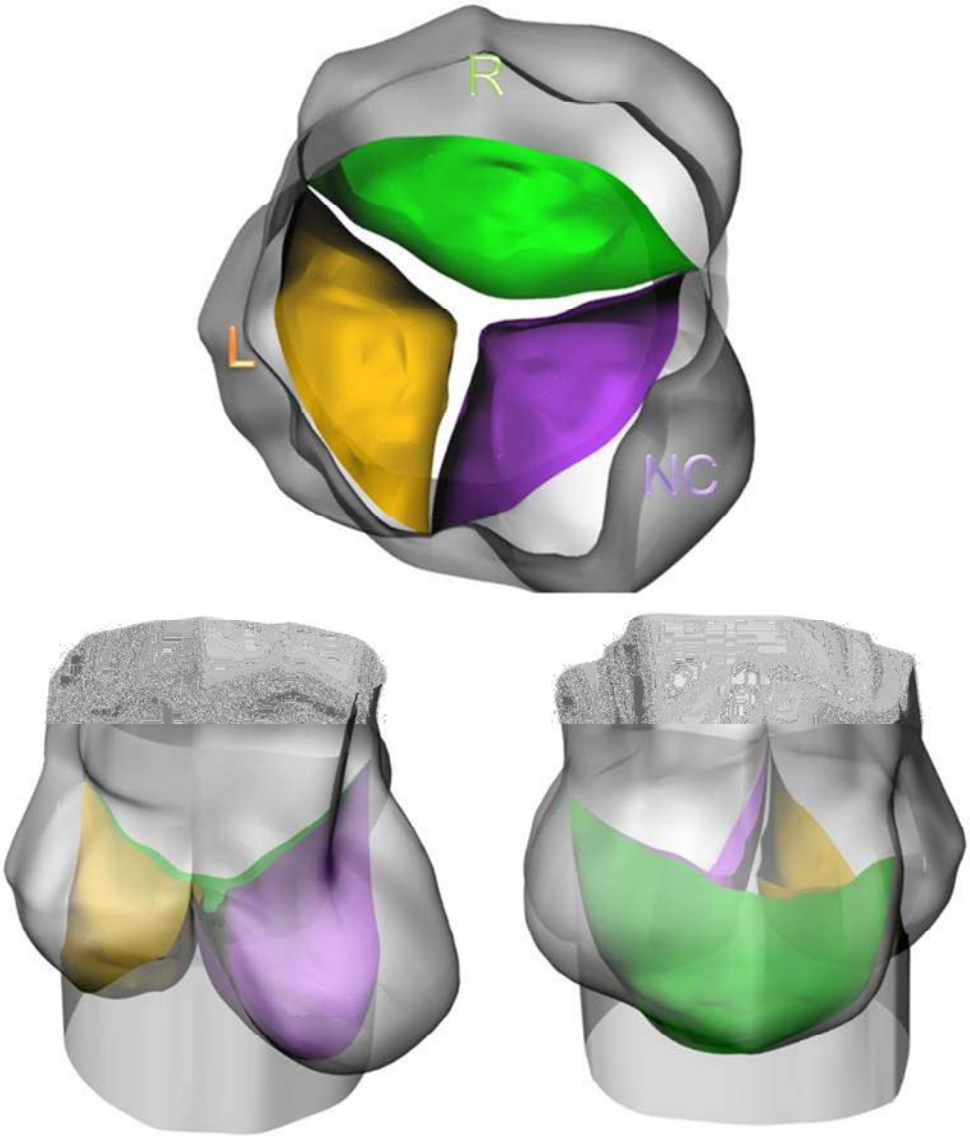

Figure 5. Leaflet and sinus views of TAV1.

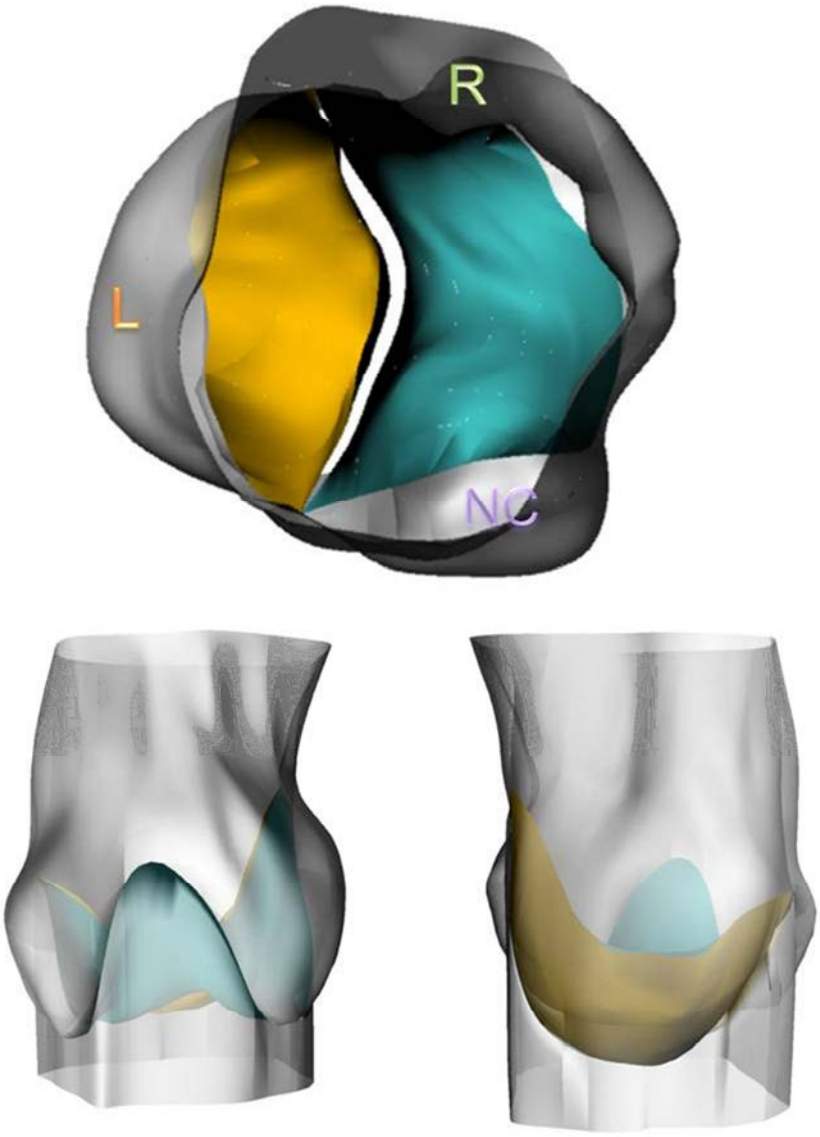

Figure 6. Leaflet and sinus views of BAV1. The noncoronary and right leaflet form the conjoint cusp in this patient.

Table 1. Geometric areas of the leaflets for each valve. The fused leaflet of the BAV is indicated by the sections that have been connected.

	Left Leaflet Area (mm^2)	Right Leaflet Area (mm^2)	Noncoronary Leaflet Area (mm^2)
TAV1	**286**	**334**	**351**
TAV2	257	382	376
TAV3	**456**	**408**	**287**
TAV4	356	250	322
TAV5	**291**	**300**	**290**
BAV1	544	682	
BAV2	**438**		**372**
BAV3	353		347

The size trend of the geometric leaflet surface area is left < right < noncoronary in TAV1. This trend matches those expected to be observed in normal human aortic valves [9-10]. The other valves pose trends as follows: TAV2 and TAV5 left < noncoronary < right, TAV3 noncoronary < right < left, TAV4 right < noncoronary < left. In all the BAV cases the fused leaflet is larger than the single. BAV1 represents a morphology that is known to occur with a frequency near 5% [31]. The morphology of BAV1 can be described as a fusion of the right and noncoronary leaflets, which in this thesis will be referred to as Type 2. The left coronary leaflet is fully formed but may be pathological in size. BAV2 and BAV3 represent a more common morphology and occur with a frequency in nearly 39% of patients who have a bicuspid valve [31]. This morphology results in fusion of the left and right coronary leaflet, and for this

analysis will be referred to as BAV Type 1. On average, the coaptation percentages of all the valves are greater than 30%, which clinically is considered the minimum [9-10, 40]. Medical records of the patient data received indicated all TAV(1-5) had some sort of other complication; the patients of BAV(1-3) were under supervision due to bicuspid valve presence. This information can be found in Table 1.

3.3 Geometrical Validation

After model generation, an analysis of the final TAV1 and BAV2 valve dimensions was completed by comparing the data from the reconstructed geometry with those directly obtained from rt3DE images. Results of this comparison are shown in Table 2 and Table 3, respectively. On average, the variation of the reconstructed geometry versus the image data shows good agreement. A maximum variation of 20% was measured in TAV1. For BAV1, the maximum variation was 18%. The overall accuracy of the model can be qualitatively assessed by superimposing the original data on the final data, as shown in Figure 7. Looking at the surfaces relative to the surrounding point cloud, there is good agreement.

Table 2. Measurements (mm) used to validate relevant dimensions of patient TAV1.

Measurement	TAV								
	Right			Left			Non		
	Jermihov	RT3D	% difference	Jermihov	RT3D	% difference	Jermihov	RT3D	% difference
Intercommisural diameter	23	22	5	20	21	-5	21	21	0
Annular diameter	23	25	-8	20	25	-20	20	25	-20
STJ diameter	22	26	-15	20	23	-13	21	23	-9
Height of the sinuses	19	20	-5	15	17	-12	21	19	11

Table 3. Measurements (mm) used to validate relevant dimensions of patient BAV1.

Measurement	BAV								
	Right			Left			Non		
	Jermihov	RT3D	% difference	Jermihov	RT3D	% difference	Jermihov	RT3D	% difference
Intercommisural diameter	27	27	0	27	29	-7	30	26	15
Annular diameter	29	31	-6	27	27	0	27	33	-18
STJ diameter	26	29	-10	26	30	-13	24	28	-14
Height of the sinuses	21	24	-13	19	23	-17	22	23	-4

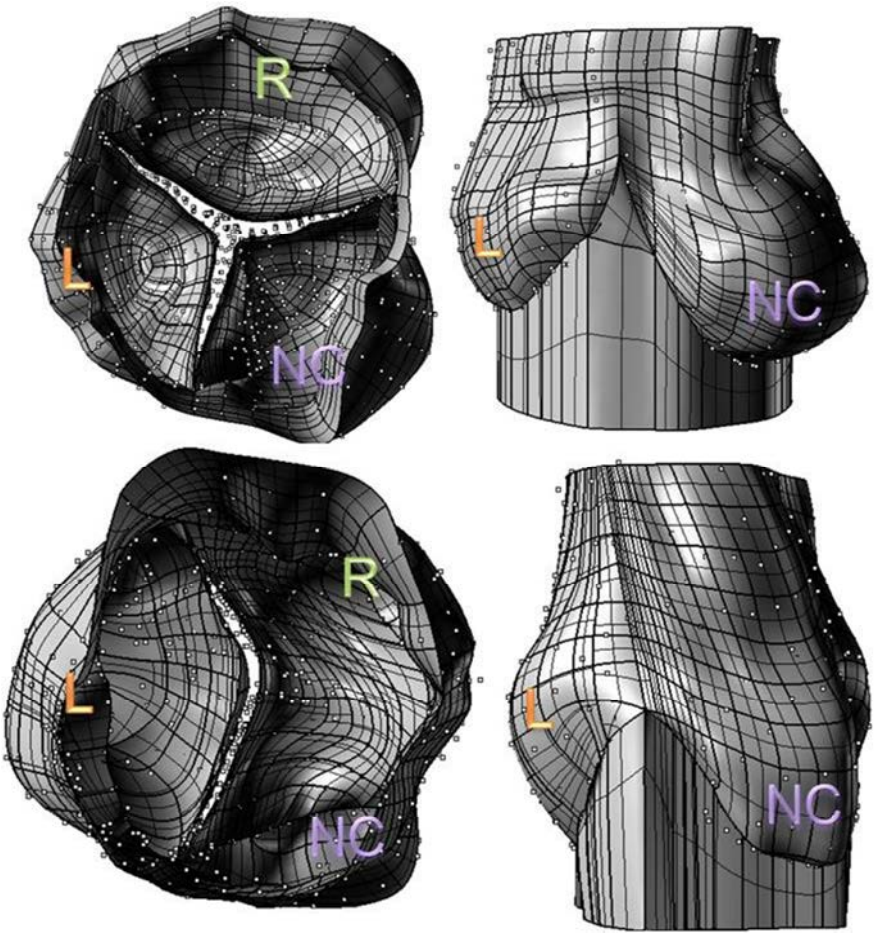

Figure 7. To compare the completed geometry and the initial patient point cloud data, the two are shown superimposed on one another (TAV1 above and BAV1 below).

CHAPTER FOUR: MECHANICAL ANALYSIS FORMULATION

4.1 Continuum Mechanics

Continuum mechanics is the theory behind a FE analysis. This section will briefly review basic theories of deformation of solids and kinematics of motion.

4.1.1 Finite Deformation of Solids

In the theory of solid deformation, an arbitrary material body can be viewed as a collection of "particles" that are defined in a region, $\mathcal{B}$, of Euclidean space $\mathbb{R}^3$. The original, or reference, coordinate points are denoted by vector X_j. The three components of the reference, or local, coordinates are commonly defined in a Cartesian coordinate system $\{E_1, E_2, E_3,\}$ existing in $\mathcal{B}$. Uppercase lettering will assume reference configuration and lowercase the current configuration. Therefore, any particle of the material body defined in $\mathcal{B}$ is:

$$X= X_1E_1+X_2E_2+X_2E_2 \qquad (4.1)$$

A given particle that has displaced in time is represented by its current coordinates, x_j. The notation for this displacement as a function of time is:

$$x=\varphi(X, t) \qquad (4.2)$$

The function simply transfers the reference coordinates X_j to a new position x_j, with respect to time. The new, or current coordinates, can be defined in a separate coordinate system $\{e_1, e_2, e_3,\}$ existing in $\mathcal{B}$ and is described by:

$$x= x_1e_1+x_2e_2+x_2e_2 \qquad (4.3)$$

It is important to note that there is a one-to-one correspondence between the mapped and reference coordinates, denoted by $\varphi:\mathcal{B} \rightarrow \mathbb{R}^3$. This condition implies that there are no cracks or singularities in the problem. By taking two particles in a reference coordinate system defined as A and A' that are an infinitesimally small distance apart, ΔX, are transformed to current coordinates by the line image:

$$\Delta x = \varphi(X + \Delta X) - \varphi(X) \tag{4.4}$$

written in differential form:

$$dx = \frac{\partial \varphi(X,t)}{\partial X} dX \tag{4.5}$$

The tangent tensor denoted by F represents the deformation gradient shown in equation (4.6).

$$F = \frac{dx}{dX} = \frac{\partial \varphi(X,t)}{\partial X} \tag{4.6}$$

The gradient transforms vectors defined in the reference configuration to that of the current configuration [41].

4.1.2 Stress and Strain Definition

To properly quantify the strains present in the leaflet during the full cycle, a finite definition of strain is needed. Green's strain tensor will link the kinematic analysis and the constitutive model. Green's strain tensor does not require calculation of principal directions; it can instead be obtained directly from the deformation gradient, , making it attractive for rapid computation [41]. The right Cauchy-Green tensor is defined as:

$$C = F^T F \tag{4.7}$$

Thus, Green's strain tensor is defined as:

$$\varepsilon^G = \frac{1}{2}(C - I) \qquad (4.8)$$

is identity tensor in equation 4.8 [41]. The strain measure used in this study is logarithmic strain defined as:

$$\varepsilon = \frac{1}{2}\log C \qquad (4.9)$$

Logarithmic strain is used as measure for its accuracy in large deformation problems; it is also generally accepted as an effective means to evaluate strain magnitudes in the valve leaflet [19, 41-42].

The stress used for numerical calculation is the Cauchy stress, which is a representation of true stress because it is defined by the force per unit area in the current configuration rather than the reference configuration. The Cauchy stress is related to the 2nd Piola-Kirchhoff stress.

$$\sigma = \frac{1}{J}FSF^T \qquad (4.10)$$

J is the determinant of deformation gradient. In finite strain elasticity is derived from a strain energy function.

4.2 Balance Equations

Newton's second law is followed in the motion of an arbitrary body in current coordinates. The material body has volume, V which is bound by surface S. The balance equation is simply the sum of traction vector forces, t_i acting on the surface bounding the volume and body forces b_i acting on the volume shown in equation 4.11.

$$t_i = \sigma_{ij} n_i \qquad (4.11)$$

The integral of the traction vector forces summed with the integral of the body forces times the mass density, ρ, equals the integral of total mass density times acceleration, $\ddot{u}_i$. This is an acceleration component. A weak form can be derived through multiplication of the local form of the balance of linear momentum by an arbitrary weighting function w_i and carrying out the integration. For the final form, the traction boundary condition (4.11) needs to be substituted. These steps result in the following equation

$$\int_V \rho w_i \ddot{u}_i \, dV + \int_V w_{i,j}\sigma_{ij} \, dV = \int_S w_i t_i \, dS + \int_V w_i \rho b_i \, dV \tag{4.12}$$

This formulation of the balance equation is known as the weak form. The weak form is also known as the principle of virtual power [41]. It is important to note the distinct advantage associated with the principle of virtual power formulation. There only exists the first derivative of u_i implying the solution may be more general so long as the integrals work mathematically [41]. The enforcement of boundary conditions also changes with the weak formulation. The traction boundary conditions are satisfied weakly, and the essential boundary condition are satisfied strongly.

4.3 Finite Element Formulation

This section will introduce the FE formulations used to solve the complex problems required of this analysis. The software package used for this study is ABAQUS/Explicit, which will mainly be solving the complex differential equation. The goal of the FE equations is to discretize the kinematic quantities for use in the principle of virtual power [41].To begin with, displacement, u, is interpolated by:

$$u = Nd \tag{4.13}$$

Where 0 is the element nodal shape functions and d is the element nodal displacement vector. Using the assumed displacements, elemental strain can be derived using the nodal strain-displacement matrix 1 4.14. For transient problems:

$$\ddot{u} = N\ddot{d} \tag{4.14}$$

$\ddot{d}$ is the vector of nodal accelerations, B contains shape function derivatives. In accordance with the Galerkin method of weak form derivation, at the element level the following relationships are derived:

$$f^{int} = \int_{\Omega_e} B^T \sigma dv \tag{4.15}$$

$$M = \int_{\Omega_e} \rho N^T N dv \tag{4.16}$$

$$f^{ext} = \int_{\Omega_e} N^T \rho b dv + \int_{\partial\Omega_e^t} N^T \bar{t} da \tag{4.17}$$

Ω_e is the domain of a single element [41]. With these derived terms, the elemental equations can be written:

$$M\ddot{d} + f^{int} - f^{ext} = 0 \tag{4.18}$$

The global equation is obtained by assembling element equations.

4.4 Explicit vs. Implicit Solution Method

ABAQUS is able to form FE solutions via implicit (ABAQUS Standard), or explicit (ABAQUS/Explicit) numerical methods. Solution method selection depends on the specifics of the problem. Generally, implicit formulation is the preferred method, because equilibrium of

the balance equation is enforced at every time step. This is not the case with explicit formulation, which approximates the displacement of the next time step using the acceleration of the current time step. This approximation may introduce inaccuracies and stability issues, whereas implicit formulation yields results of high accuracy and no stability issues [43]. Steep pressure gradients, short duration of the cardiac cycle, and large deformations make explicit formulation attractive for this analysis. When conditions such as these are present, choosing an explicit analysis is favorable. The explicit formulation is conditionally stable dependent on time step size [43]. ABAQUS/Explicit uses a central-difference integration rule to solve the equation of motion, previously defined. In an ABAQUS/Explicit analysis the mass matrix, M, is diagonalized or "lumped." This diagonal "lumped" mass matrix is easier to invert and can be applied directly to the equation of motion to solve for acceleration $\ddot{u}$.

$$\ddot{u}^{(i)} = M^{-1} \cdot (f_{ext}^{(i)} - f_{int}^{(i)}) \qquad (4.20)$$

The acceleration is used to compute the velocity at the next time step. With the velocity computed, the displacement, u, can be found. It is important to note the existence of the current velocity term $\dot{u}^{(i-\frac{1}{2})}$ in the equation 4.21. This value is computed through a separate equation set incorporating prescribed initial boundary conditions [43].

$$\dot{u}^{(i+\frac{1}{2})} = \dot{u}^{(i-\frac{1}{2})} + \frac{\Delta t^{(i+1)} + \Delta t^{i}}{2} \ddot{u}^{(i)} \qquad (4.21)$$

The displacement equation in 4.22 results. With displacement known, strain

$$u^{i+1} = u^{i} + \Delta t^{i+1} \dot{u}^{i+\frac{1}{2}} \qquad (4.22)$$

increments, element stresses, and internal forces can be computed. The time step sizes were automatically calculated by ABAQUS/Explicit. During an explicit analysis the time step size is computed for each step based on stability criteria (4.23).

$$\Delta t \leq \frac{2}{\omega_{max}}(\sqrt{1+\xi^2}-\xi) \tag{4.23}$$

ω_{max} is the highest frequency of the system, and ξ is the highest mode fraction of critical damping [43]. ABAQUS uses built-in algorithms to compute these values prior to each step to generate a stable time increment [43].

CHAPTER FIVE: FE ANALYSIS

5.1 Material Properties

FE simulations of biological tissue are continuously evolving. A particular path of this evolution can be seen in the modeling of heart valves. One of the first FE heart valve simulations was conducted by Catalogue et al. (1977), implementing a linear isotropic material model [44]. This initial study precipitated FE methods applied to heart valve research. Major advances in this field involve proper material model establishment and implementation. Experimental studies have revealed anisotropic and nonlinear material behavior in the biological tissues that comprise the heart valve leaflet [1, 12-14, 18, 23-26]. These properties arise from the complex microstructure inherent in biological tissue [18, 23-26]. Valve tissue is composed of several layers, including an assortment of collagen and elastin fibers oriented circumferentially. In a resting unloaded state, some of the fibers will be irregular; as tension is applied the fibers will reorient and elastic fibers will unfold, all dependent upon loading [1-2, 23-26]. The fiber orientation and corresponding direction on the leaflet used for this analysis is shown in Figure 8.

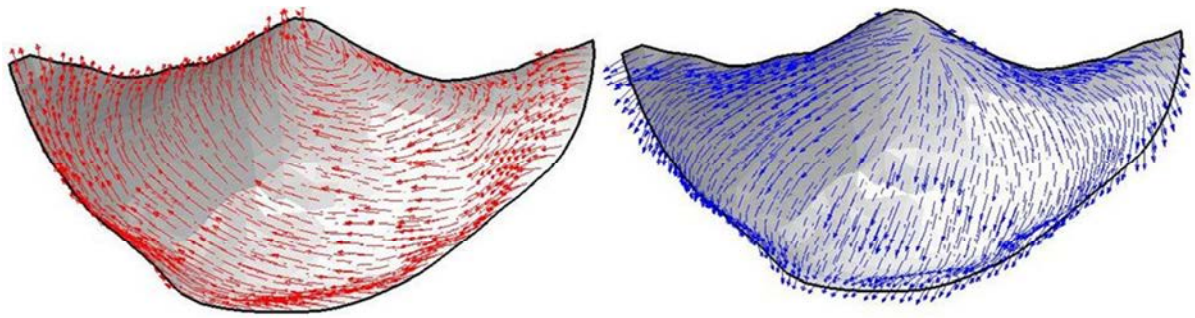

Figure 8. Fiber directions assigned to the leaflets. Circumferential and radial, red and blue, respectively.

Gnyaneshwar et al. (2002) have conducted a dynamic FE analysis including full leaflet contact and the aortic root, presenting a vast improvement over initial simulations such as that of Catalogue et al. (1977). Accuracy of FE simulations employing biological tissue models has increased, thus increasing the efficacy of the results.

Several forms of material anisotropy for soft and biologic tissue in computational analysis have been developed, including transverse isotropy, orthotropy, and structural constitutive models [25-26]. A widely accepted energy model is the Fung exponential model, developed by Fung et al. (1979) [19, 42, 45]. The fully anisotropic 3D strain energy function of the Fung model is defined by equations 5.1 and 5.2 [19, 42]

$$W = \frac{c}{2}[e^{Q} - 1] \quad Q = \mathrm{E} \cdot \mathrm{DE} \tag{5.1}$$

$$Q = b_1E_{11}^2 + b_2E_{22}^2 + b_3E_{33}^2 + b_4E_{11}E_{22} + b_5E_{11}E_{33} + b_6E_{22}E_{33} + b_7E_{12}^2 + b_8E_{13}^2 + b_9E_{23}^2 + b_{10}E_{11}E_{12} + b_{11}E_{22}E_{12} + b_{12}E_{33}E_{12} + b_{13}E_{11}E_{13} + b_{14}E_{22}E_{13} + b_{15}E_{33}E_{13} + b_{16}E_{12}E_{13} + b_{17}E_{11}E_{23} + b_{18}E_{22}E_{32} + b_{19}E_{33}E_{23} + b_{20}E_{12}E_{23} + b_{21}E_{13}E_{23} \quad (5.2)$$

In the current study, an extension of the original Fung model was implemented and defined by strain energy function N of equation 5.1. The six in-plane material parameters experimentally derived by Sacks et al. (1998) have been used; the remaining 15 material parameters involving out-of-plane deformation were approximated similar as in-plane, however, some of the parameters have been reduced . This approximation is based on the assumption that out-of-plane deformation will have minimal effect on in-plane deformation. There is no experimental verification available for the approximate parameters. The constants used to define the fully anisotropic model in equation 5.2 are listed in the equations of 5.3. In equation 5.2, b_i are the material constants associated with the material directions E_{ij} . Q is a function of strain composed of the Green-Lagrange strain tensor E and material anisotropy tensor D. Constant c is the stiffness parameter that has been previously determined experimentally by Sacks et al. (1998). The thickness assigned to the shell elements of the leaflets was 0.6 mm, which represents an average for normal human aortic valve leaflet tissue

[9-10]. The tissue was approximated as incompressible, an assumption that arises from the high water content and low permeability of biological tissue, d. The compressibility constant is assumed small enough to maintain this approximation [23-26]. These constants were derived from biaxial testing of fresh porcine aortic valve leaflet tissue, the closest known analog to normal human valve tissue.

b_1=	49.558	b_9=	8.02	b_{17}=	-0.002	
b_2=	5.2871	b_{10}=	-0.004	b_{18}=	-0.01	
b_3=	24.779	b_{11}=	-0.02	b_{19}=	-0.002	
b_4=	-3.124	b_{12}=	-0.002	b_{20}=	-0.002	(5.3)
b_5=	24.779	b_{13}=	24.779	b_{21}=	-0.002	
b_6=	-1.56	b_{14}=	-0.01	c=	9700	
b_7=	16.031	b_{15}=	24.779	d=	1e-6	
b_8=	24.779	b_{16}=	-0.002			

The aortic valve leaflets move through a blood medium that is of similar density to the leaflet itself; however, damping exists during this motion due to the viscous forces. Previous studies, including that of Kim et al. (2007), have applied a clinically verifiable damping constant with success in producing proper valve motion [12-14]. However, ABAQUS currently lacks support for damping application to fully anisotropic materials. To circumvent this issue, the current study has applied a skin layer of St. Venant isotropic material specification of shell elements type S3R. Also included in this skin layer was a damping coefficient. This skin was applied to the aortic side of the leaflet surfaces. A visual schematic of how the skin is applied to the surface is shown in Figure 9. The skin uses the same underlying mesh of the leaflet surface, and there is no relative motion between layers.

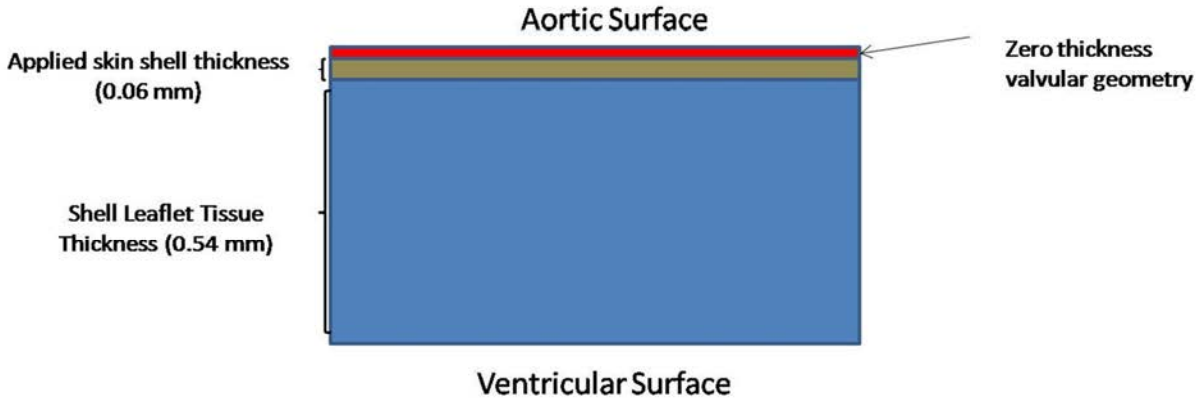

Figure 9. Illustration of skin application used for mass proportional damping coefficient implementation to account for the viscous force dissipation by the blood.

The purpose of the skin in this study was to introduce damping. The skin has a thickness of 0.06 mm and is defined with St. Venant-Kirchoff isotropic material properties with parameters E = 1000Pa, ν = 0.3, ρ = 1100 $\frac{\text{kg}}{\text{m}^3}$ and a mass proportional damping constant alpha of 90000 s^{-1}. Damping in ABAQUS/Explicit is defined by [C] = α[M] + β[K]. [C] is the damping matrix, [M] the diagonalized mass matrix, and [K] the stiffness matrix. Alpha is the mass proportional damping constant of the damping matrix used by ABAQUS/Explicit. This equation yields a damping matrix of units g/s . This constant does not have an experimental comparison; instead, it was established through qualitative motion analysis of the leaflet in

which proper opening and closing times were observed. This resulted in a peak open orifice near 0.14 seconds, and fully closed configuration at 0.3 seconds. These values are similar to previously computed opening and closing times of Kim et al., which opened at 0.09 seconds and closed at 0.3 seconds, respectively [12-14]. Previous studies have concluded that a small variation of leaflet thickness will have a minor effect on stress [14]. The sinus and annulus structures were assigned the same density as the leaflet tissue, but a linearized isotropic material model was utilized due to lack of mechanical testing data. The Young's modulus used for the sinus and annulus was equal to 2 MPa, but the shell thickness was assigned averaged human physiological values of 2.31 mm and 2 mm, respectively [9-10].

5.2 Boundary Conditions

To most effectively capture the in vivo conditions of the aortic root, the uppermost boundary of the root along with the lower boundary were fixed from moving longitudinally. To eliminate rigid body rotation, a single node at the top of the sinus was fixed in all degrees freedom. To prevent excessive translation/rotation of the valve within the root, two additional nodes at the top and bottom were fixed in only a single in-plane direction. The free edges of the leaflets are unrestricted. An illustration of these boundary conditions on a TAV model is shown in Figure 10.

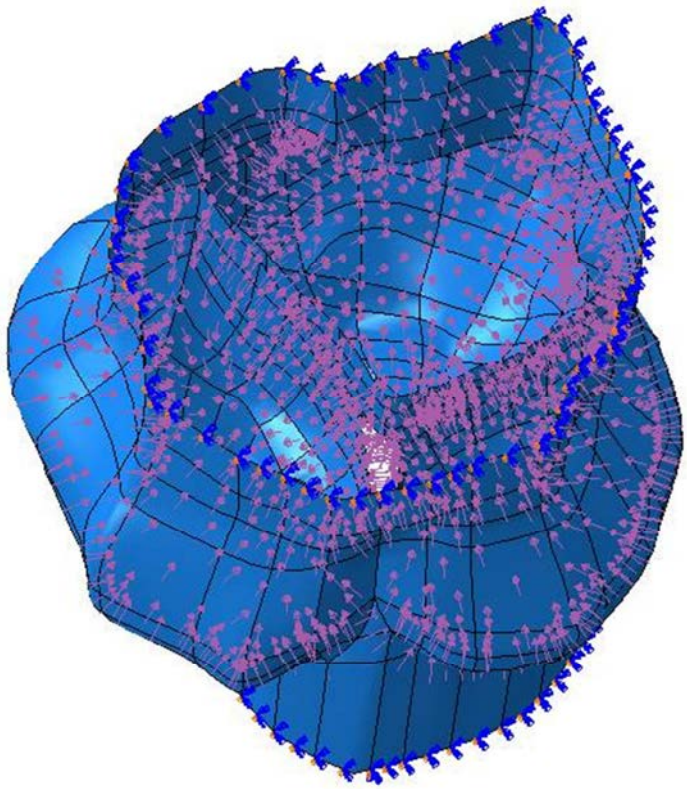

Figure 10. Illustration of applied boundary conditions. Pressure loading applied to the leaflet and root structures. The top and bottom are fixed from axial translation along with additional nodes, preventing rigid body rotation as well as excessive rotation of the valve within the root.

The pressure difference versus time curve shown in Figure 117 is an approximation of the full cardiac cycle, representing the difference between left ventricular and aortic pressure. This pressure difference was applied to the leaflets and the sinus. The leaflets open under a pressure of 4 mmHg, which reduces to 0 mmHg at 0.2 seconds at end systole. A large negative pressure pulls the leaflets toward closure. Both the fixation of degrees freedom and pressure

loads are depicted in Figure 10. Penalty contact method was employed in a general contact scheme where all surfaces make rigid contact. It was also specified that the leaflets were free to separate after the contact. The coefficient of friction was specified as 0.05, similar to that of Conti et al. [15-16] and employed using the Penalty technique. "Normal behavior constraint method" was left as default and pressure-over closure was "Hard contact." The resulting geometries were each meshed in ABAQUS/CAE using triangular shell elements; nodal spacing was held constant at 0.8 nodes per millimeter, and the resulting meshes are shown in Figure 12.

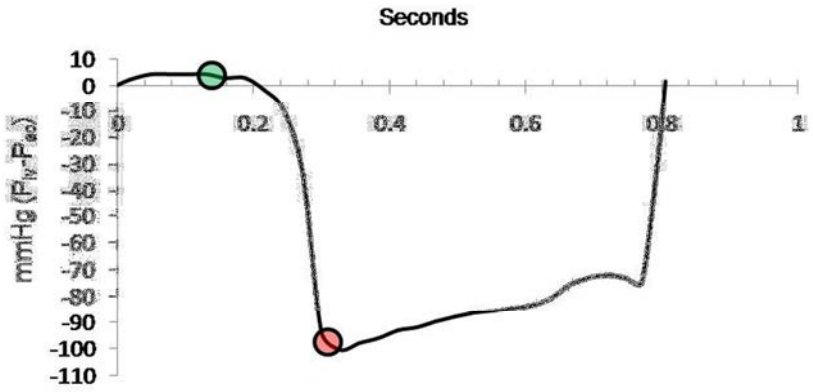

Figure 11. Time varying pressure load applied to the leaflets and root structures. Representative of the pressure differential experienced by the root and leaflets during the cardiac cycle. Green highlighting indicates mid-systole or when the valve is fully open, and red indicates full closure.

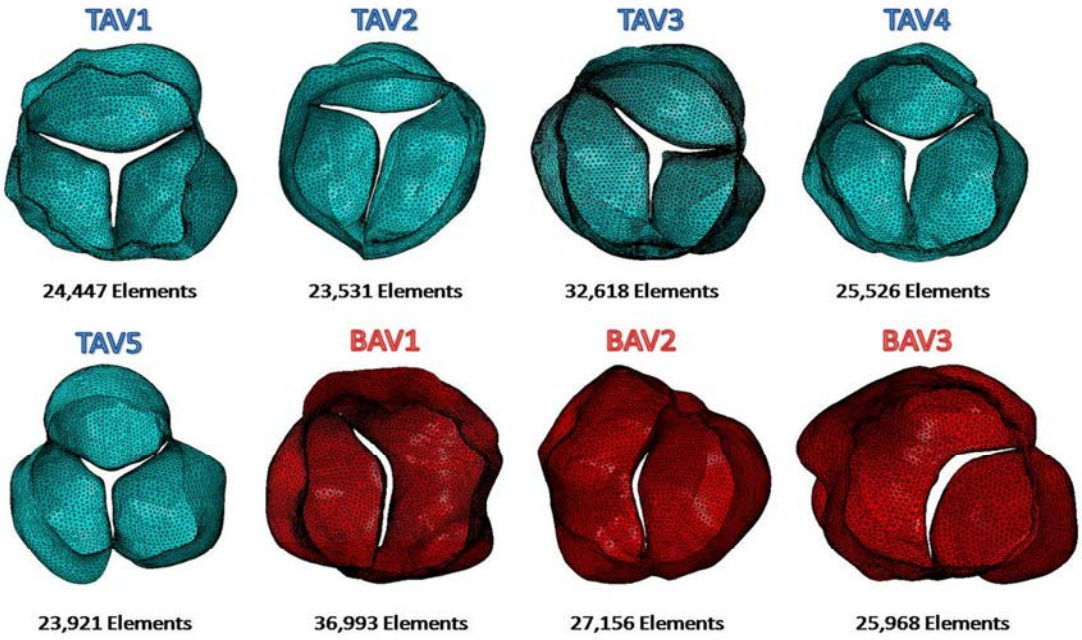

Figure 12. All geometries were meshed using triangular shell elements on nodes generated with a spacing of 8 nodes per 10 millimeters.

5.3 Results

Figures 13-16 summarize the images captured from each patient and show the motion undergone by the leaflets. The initial frame in Figure 13 shows the leaflets in the fully closed configuration from the previous cardiac cycle. When the pressure in the ventricle exceeds that of the aortic, the leaflets begin to open, as shown in Figure 14, corresponding to 0.01 seconds into the simulation. At 0.07 seconds, shown in Figure 15, the leaflets are approximately halfway to reaching the fully open configuration. The leaflets move slightly more and reveal the fully open configuration at 0.14 seconds into the simulation, shown in Figure 16. The EOA of each valve was computed by first identifying the proper plane for extraction. For each valve, a plane parallel to the annular area was extracted at the peak of the free edge. An example of

these areas is shown in Figure 17. The GOA of each valve was identified as the annular area. Each of these planar areas was extracted using ImageJ (U. S. National Institutes of Health, Bethesda, Maryland, USA, 1997–2012). The resulting areas are shown in Figure 18.

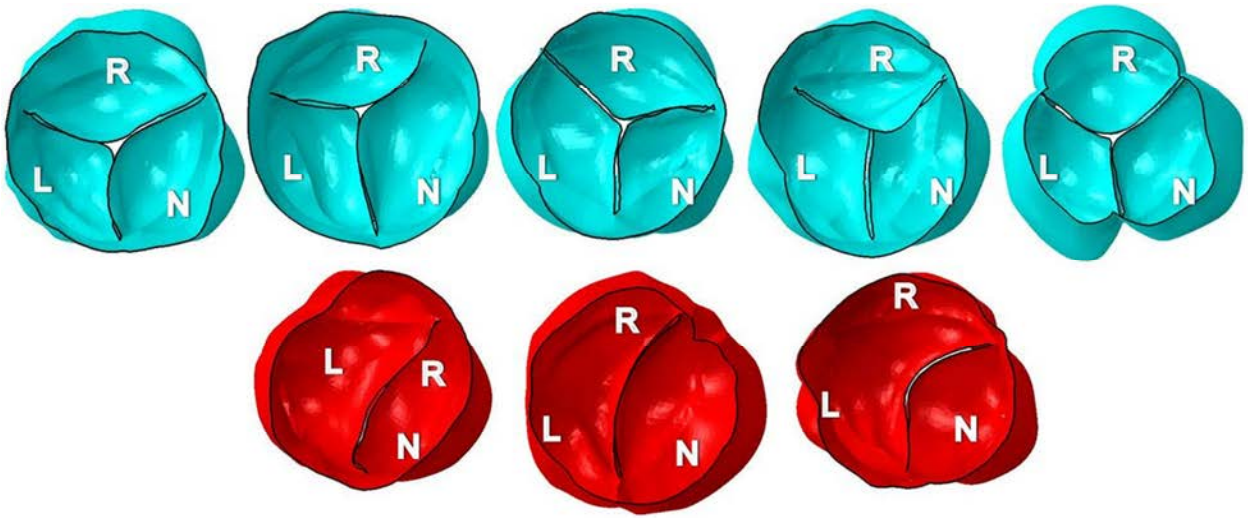

Figure 13. The valve begins in the fully closed position from the preceding cycle (end diastole).

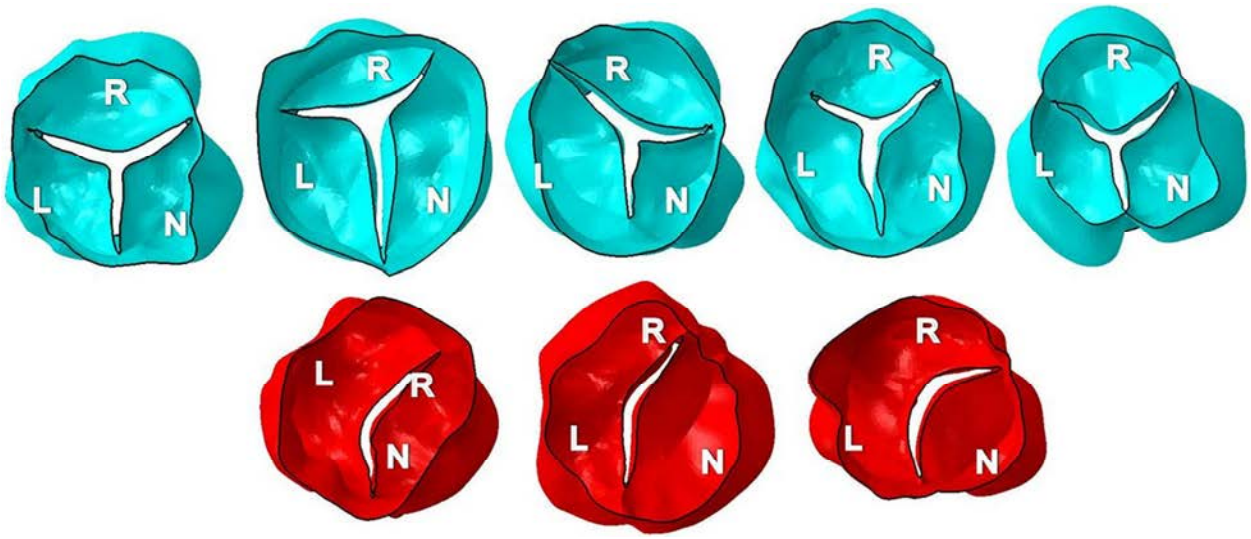

Figure 14. Transvalvular pressure begins to open the valve; time point shown is 0.001 seconds into the current analysis pressure load.

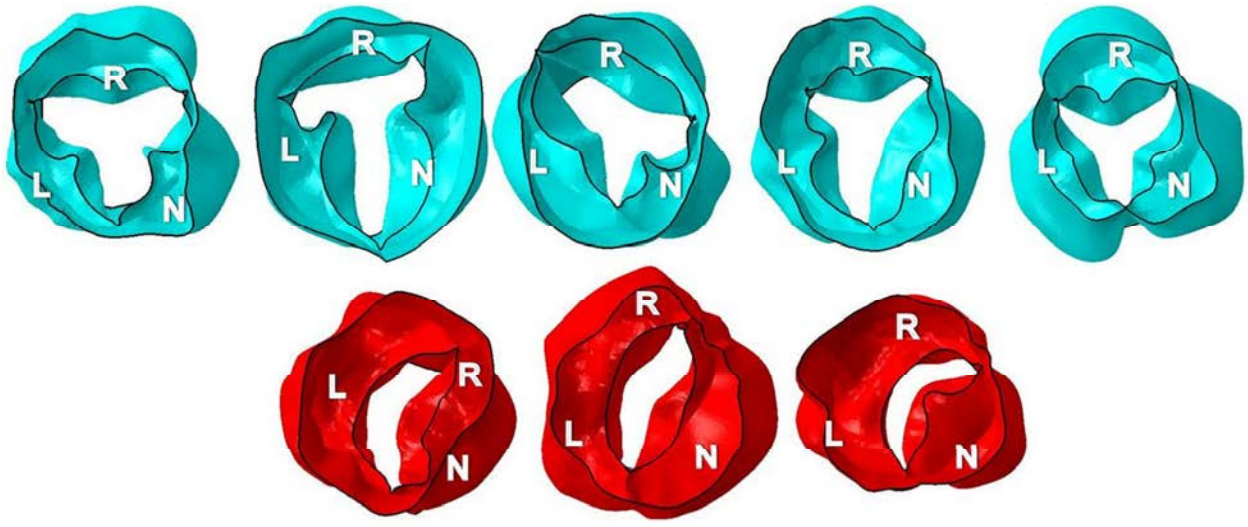

Figure 15. The valve is approximately halfway open; time point shown is 0.07 seconds into the current analysis pressure load.

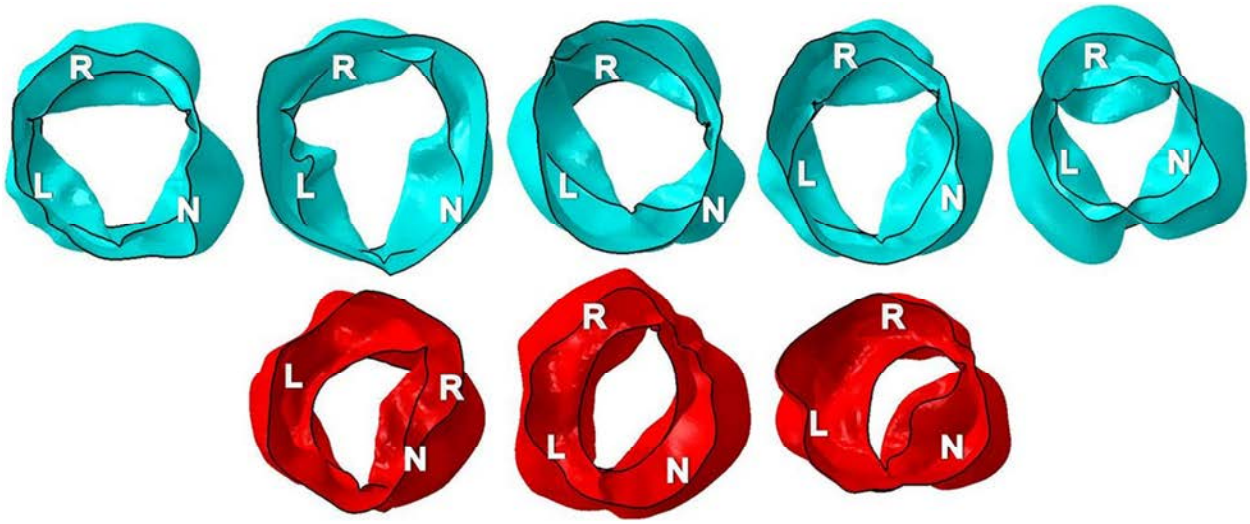

Figure 16. At this point, 0.14 seconds into the current simulation, the valves reach the fully open configuration (mid-systole).

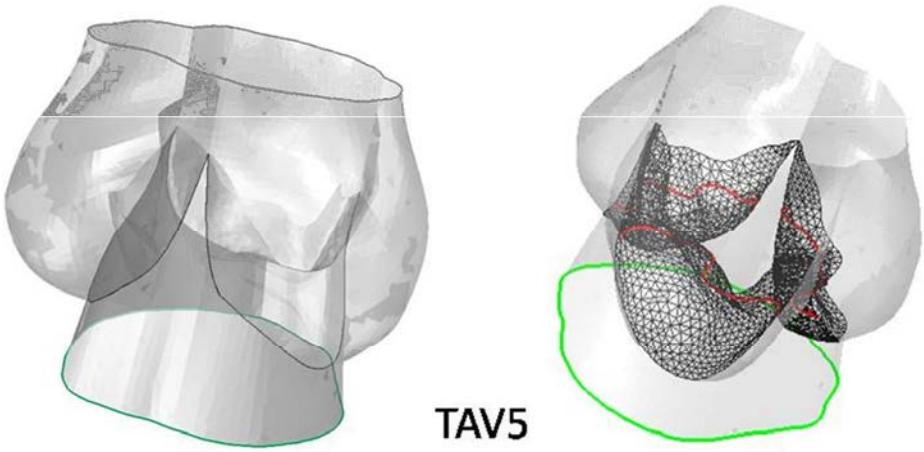

Figure 17. Illustration of EOA and GOA outlined in red and green, respectively. Shown for TAV5.

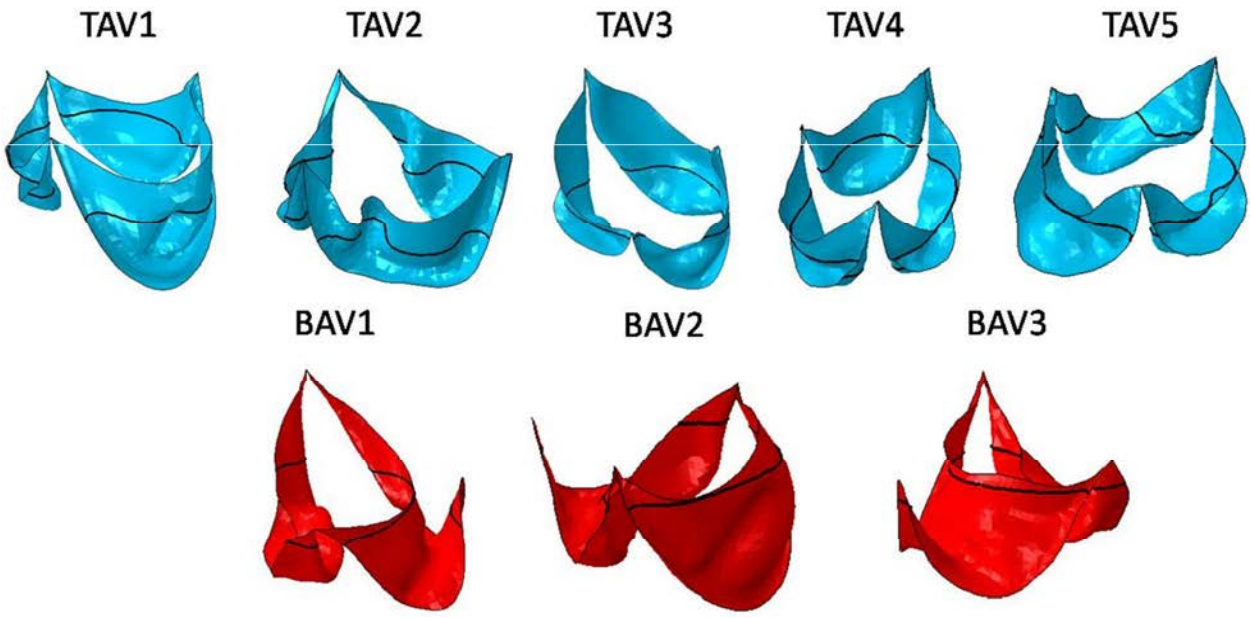

Figure 18. Planar extraction of EOA of each valve in the fully open configuration.

The primary function of the aortic valve is to allow blood passage from the left ventricle to the aorta, and hence the size of the opening created by the valve is critical. For this reason, the results concerning the opening phase are focused on orifice area in the fully open position of the leaflets. The EOA of each valve is reported in Table 2, and the corresponding contraction coefficients are shown in Table 2. However, in the fully closed configuration, the leaflets are subjected to a relatively large pressure load and are more susceptible to damage; therefore, mechanical stress is relevant.

5.3.1 Opening Phase

During the opening phase the average contraction coefficient for the TAV geometries was 0.82. To qualitatively compare the open areas of each valve, a top-down image was

captured from an aortic perspective with the leaflets in the fully open configuration, as seen in Figure 19. The TAV openings are roughly triangular. In this image the "free edge" is actually the leaflet belly as the actual free edge continues to move back towards the sinus. TAV2 displayed excessive folding of the noncoronary and right leaflets. With the BAV, two types of open area were identified: a crescent shape and elliptical. BAV1, which was of Type 2, and BAV3, which is Type 1, both revealed a crescent-shaped orifice. Despite being different morphologies, the crescent shape forms as the fused leaflet free edge draws back into the false commissure and the free edge of the un-fused leaflets undergoes a similar motion, though lesser. The elliptical orifice of BAV2 was formed in a similar manner, though the single leaflet displaced further back toward the sinus to form a larger opening. Comparing the contraction coefficients of the averaged TAV to BAV1 results in a drop of 30%, BAV2 32% and BAV3 67%.

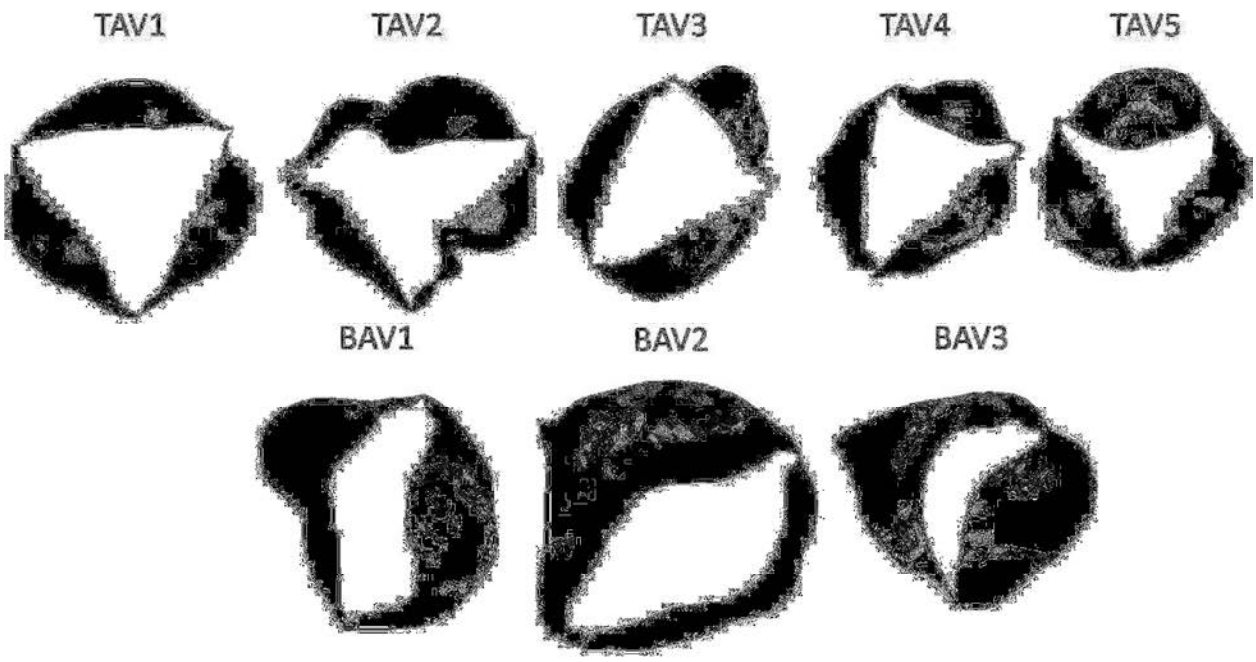

Figure 19. Top-down perspective of each valve in the fully open configuration.

It can be assumed that a more restricted orifice shape will result in abnormal flow development, which may contribute to aortic pathology.

5.3.2 Closing Phase

To ensure blood does not leak back into the ventricle during diastole, the leaflets overlap near the center. The area over which the leaflets contact each other is known as the coaptation area. An illustration of this area on TAV5 and BAV2 is shown in Figure 20, which also shows the rendered thickness. The coaptation area that was computed at full closure during the FE simulation was compared to the coaptation areas initially extracted from the patient-

specific data, as shown in Figure 21. The predicted and imaged values agree well, but TAV5 and BAV2 are outliers with a difference of 18% and 23%, correspondingly. The difference is attributed to the accuracy of the imaged data as well as how the contact area is integrated into the leaflet bellies, as previously described. Looking at the FE-predicted coaptation data, the average of all the TAV was compared against each BAV. Coaptation area was reduced by 26% in the case of BAV1, increased by 15% in BAV2, and decreased by 39% in BAV3. On average, BAV presence reduces coaptation area, although individually it may not.

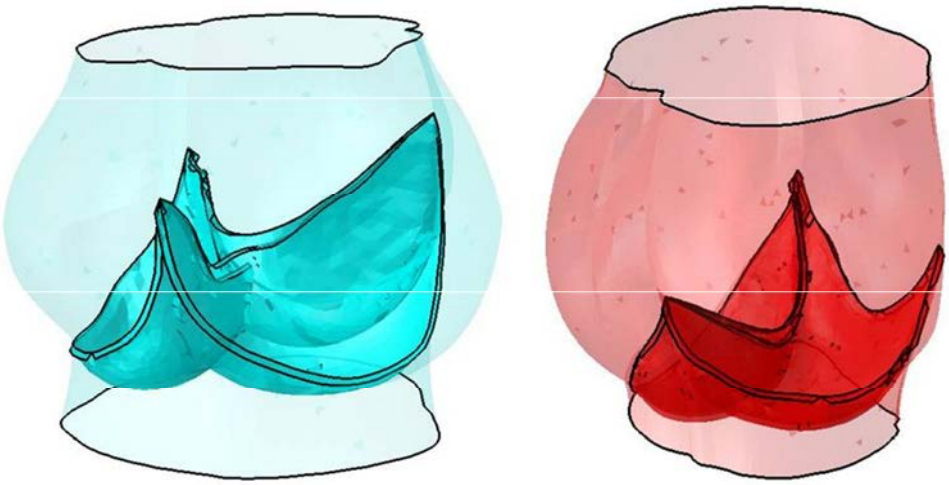

Figure 20. Leaflet coaptation at time of full closure. TAV in blue on the left, and BAV in red on the right.

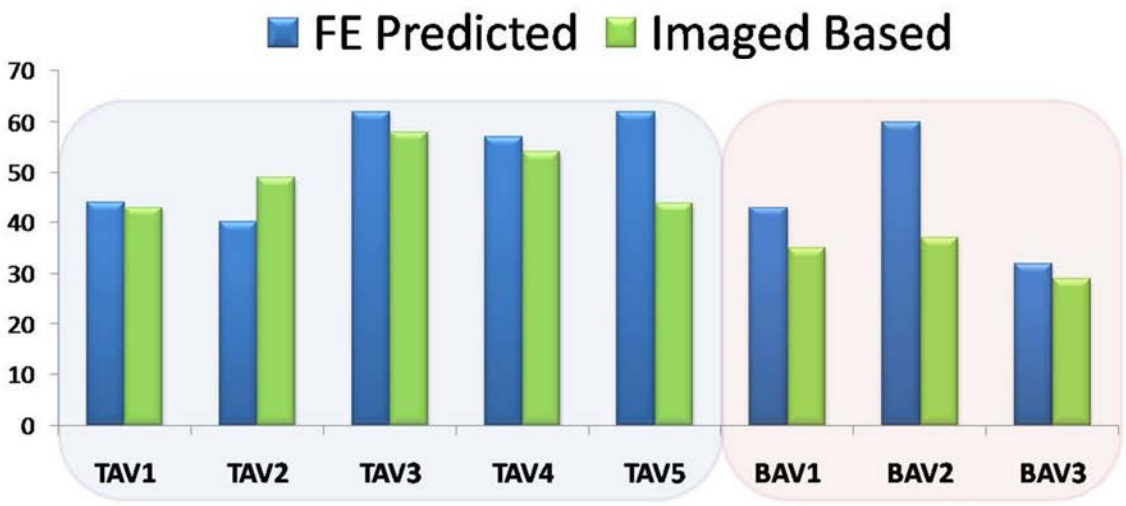

Figure 21. Results showing the computed maximum of amount of coaptation versus the area extracted from the imaged data.

The principal in-plane stress contours of the valve in the fully closed position can be found in Figure 22. Qualitatively, the BAVs analyzed in this study exhibit larger regions of high stress. BAV1 and BAV3 show stress concentration areas at the site of false commissure or fusion; the other peak stresses occur along the leaflet boundary. To more precisely understand the stress distribution of the BAV, the average, median, 95th, and 99th percentile stresses were compared as percent increases in similar values for averaged TAV. The results of the comparison are shown in Table 5. The 99th percentile shows a large increase with BAV presence. These values are directly compared with the TAV average in Figure 23. The second most common morphology, BAV1 Type 2, yielded the highest stress increase of 54%, while BAV2 and BAV3 of BAV Type 1 yielded increases of only 29% and 27%, respectively.

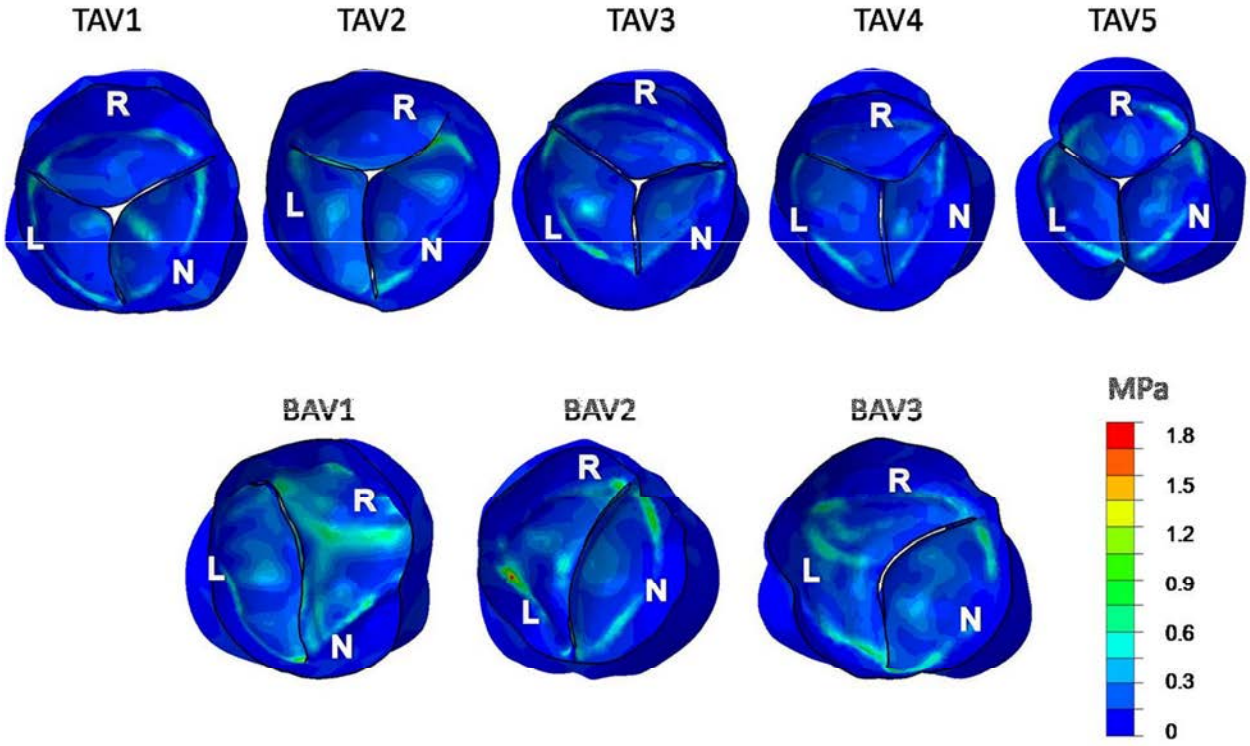

Figure 22. Maximum in-plane principal stress contours. Peak shown represents the 99th percentile stress.

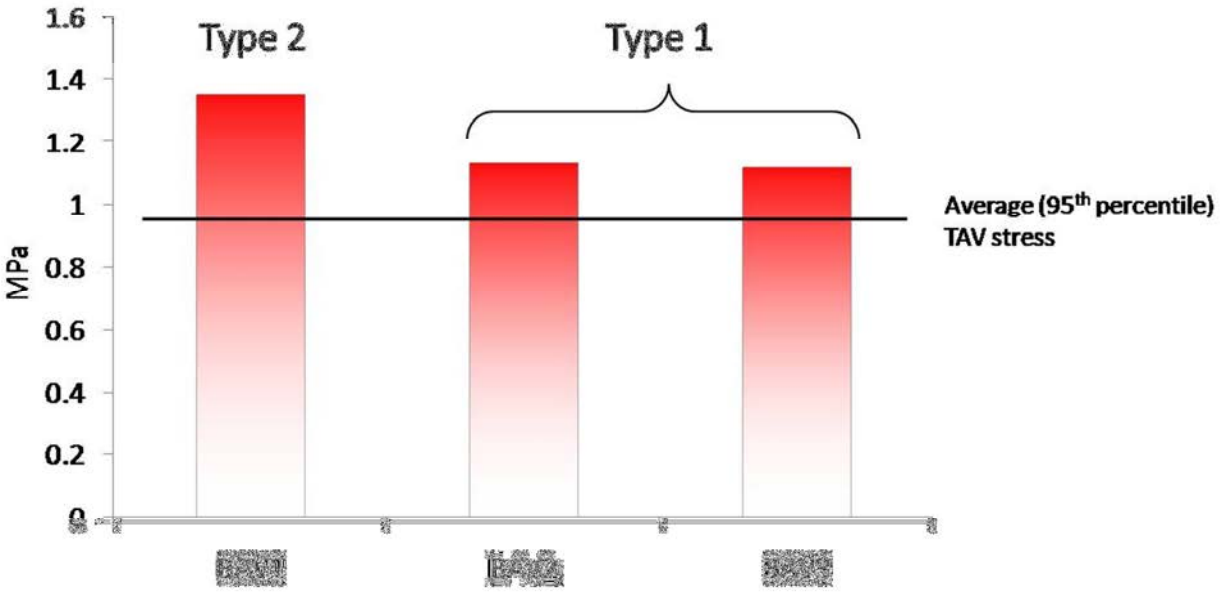

Figure 23. Maximum in-plane stress of BAV(1-3) compared to the TAV average.

Table 4. Percent increase of BAV stress from similar averaged TAV values.

	Average	Median	95th Percentile	99th Percentile
BAV1	56	55	84	93
BAV2	14	10	29	14
BAV3	-4	34	27	21

CHAPTER SIX: DISCUSSION AND CONCLUSION

6.1 Significance of the Study

For the current study to possess clinical relevance, validation of the results is necessary. The quantitative assessment of the open orifice values are used for comparison between the simulated models. However, image echo data pertaining to TAV5 and BAV2 were available. To compare the imaged results to that of the simulated images, time points corresponding to similar times in the cardiac cycle are compared. A few frames showing the majority of the free edge motion are shown in Figure 24. In this figure, the computed valve is contrasted to more clearly show similar structures to that of the image. The imaged, and predicted fully open configuration for TAV5, is shown in the top row of Figure 25. What is clear is that the belly of the leaflet in the computed configuration does not appear to coincide with the belly in the imaged configuration. However, the limited contrast of the images makes the belly region of the leaflet difficult to accurately define. The free edges are more pronounced, and a comparison can be made. For BAV2, the fully open configurations of FE predicted and echo imaged are shown in the bottom row of Figure 25. In this case the free edge is more difficult to identify, but the roughly elliptical shape can be seen. Comparing bicuspid computed and imaged data, it would appear that the predicted free edge of the leaflets does show good agreement to the same valve imaged in vivo.

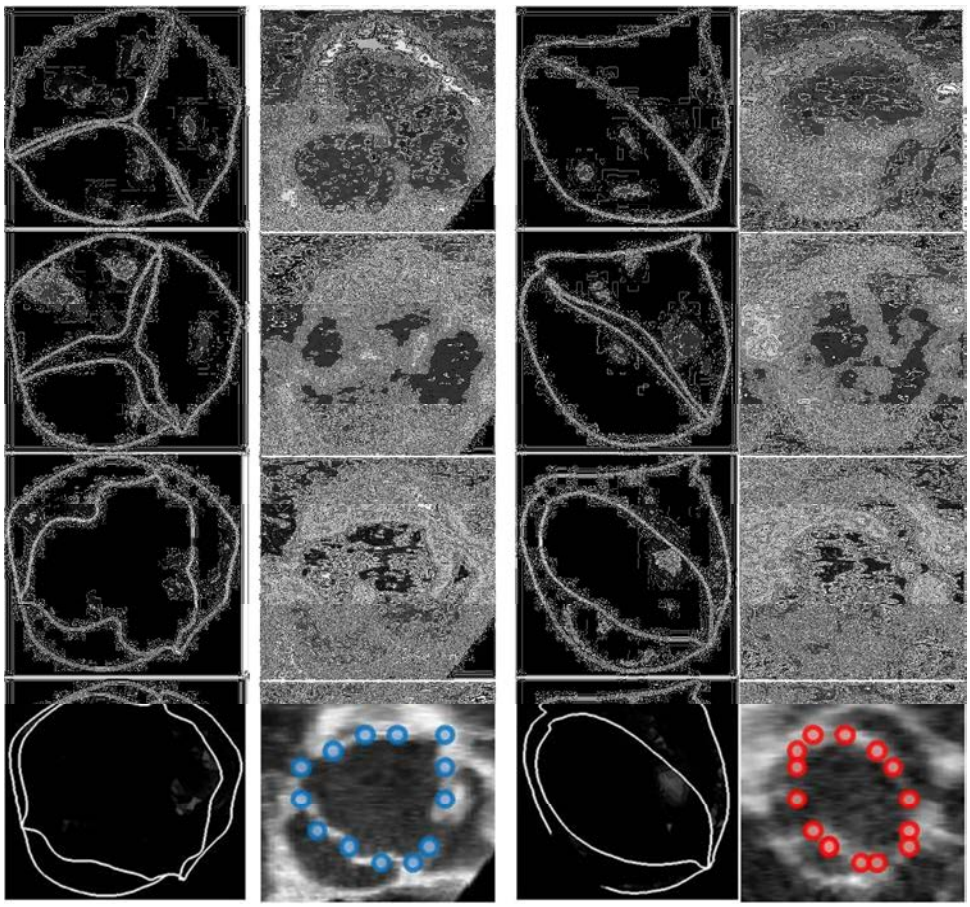

Figure 24. Side-by-side comparison of TAV5 (left) and BAV2 (right). The FE results are shown contrasted to reveal the free edge enough to compare with the echo images. The fully open configuration identified for comparison is shown in the bottom row. The orifice identified is highlighted in blue for the TAV and red for the BAV.

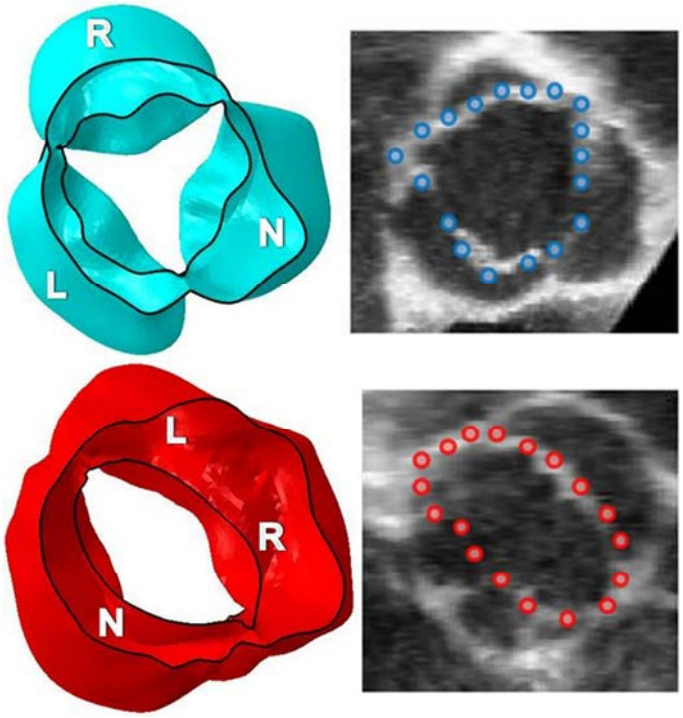

Figure 25. Full open orifice of TAV and BAV compared with the FE-predicted results (left column) and echo image of the same valve (right column).

Calcification occurs in all valves but is known to occur more rapidly in BAVs, more specifically, in the region of fusion [46]. The mechanism behind calcification has been extensively studied but not completely understood. It is generally accepted that calcification is engendered by high in-plane tensile stresses [1, 6, 13, 22, 29, 35, 47-49]. Peak stress occurs at time of full closure. As the leaflets are coapted, the back pressure from the aorta pushes the leaflets into the annulus. The 99^{th} percentile maximum in-plane principal stresses measured corresponding to TAV(1-5) and BAV(1-3) are 1.2, 1.9, 1.3, 1.2, 1.0, 1.8, 1.5, and 1.6 MPa,

respectively. The study by Jermihov et al. reported peak in-plane principal stresses in TAV and BAV as 0.2 and 0.52 MPa, respectively. In a study employing similar leaflet and sinus material properties, Conti et al. reported peak in-plane principal stresses for TAV and BAV as 0.76 and 2.9 MPa, respectively [15-16]. Considering the inherent differences between the FE simulations, the stress magnitudes obtained in the current simulation are similar for both TAV and BAV.

Given the normal size relationship for human aortic valve leaflets, noncoronary > right > left, it can be hypothesized that the ratio of the leaflet areas plays an important role in stress distribution in the leaflets and sinus structures. This relationship becomes disturbed with the presence of BAV, which will alter the stress handling capability of the structures. This analysis may help further explain the normal and pathological states of the aortic valve by identifying leaflet size ratios in TAV and BAV geometries. For this analysis, the ratio is the smallest geometric leaflet divided by the total valvular area. The resulting ratios are shown in Figure 26. The patient-specific TAV average to an area fraction of 28%, which is close to what would be expected in an ideal trileaflet valve, which is 33%. The peak in-plane principal stress of each valve was plotted against its ratio, and the results are shown in Figure 27.

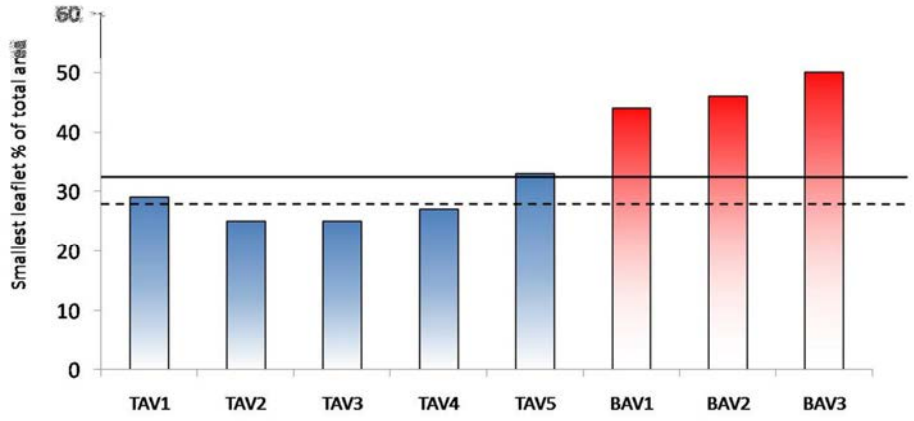

Figure 26. Smallest leaflet to total valvular surface area ratio shown in comparison to averaged patient-specific values (dotted line) and idealized fraction (solid line).

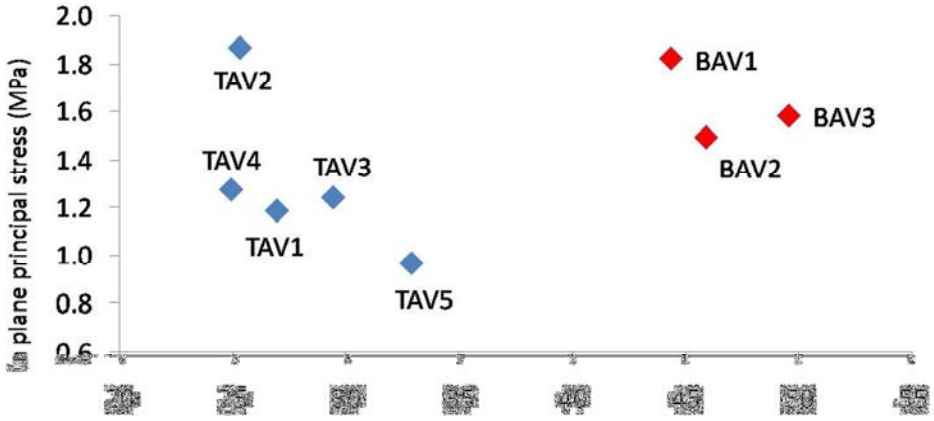

Figure 27. Plot of peak in-plane principal stress against leaflet area ratio.

Peak values of maximum in-plane stress were found in different leaflets; they consistently occurred near the leaflet attachment boundary, and more specifically, near the commissure of the adjacent leaflet. Three groups were established to describe the locations. The most common location was in the left leaflet near the commissure in common with the right leaflet, a trend shared by TAV1, TAV2, TAV4, and BAV2. It should be noted that the stress concentration in BAV2 is near the "false" commissure that would have split the fused leaflet into two. The second is on the left leaflet, near the noncoronary commissure shared by BAV1 and TAV3. In TAV5 and BAV3, the stress concentration was in the noncoronary leaflet near the commissure shared with the left leaflet.

The regions of elevated stress are more numerous and prominent in BAV. The mechanism underlying this effect could be due to abnormal leaflet stress-sharing characteristics that may manifest in the TAV but are more prominent in combination with congenital BAV. Given the asymmetry of the resulting stress along the leaflet attachment boundary, further complications may result from the skewed environment. Clinically, it may be of use to digitally reconstruct the aortic valve and assess the leaflet fraction for treatment implications prior to any computational simulations. Given the results presented in this thesis, it may be surmised that patient-specific BAV can negatively impact the surrounding physiology through altered mechanical stress during closure and/or altered hemodynamics as a result of a pathological open orifice. It should be emphasized that a trend of increased stress and restricted orifice area is present in BAV.

6.2 Limitations

The current analysis offers a unique look into the function of the aortic valve, both in normal and pathological states. The patient data collected did not provide sufficient data, so new surfaces needed to be approximated to best fit the understood geometry of the valve. This introduced areas that are artificial, such as the generation of the contact surfaces based on a single zero-thickness surface. The portion of the annulus supporting the valve was also approximated, because the provided data was limited to the base of the sinus structures. B-splines and NURBS surface patch generation varies depending on the resolution of the imaged patient valve. However, the protocol outlined in the Appendix will yield surface patches of more uniform size.

The continuity of NURBS surfaces for this analysis needs to be evaluated and constrained for a future isogeometric solid analysis. A patch stitch of 2 mm is applied when the NURBS-patches are imported into ABAQUS. The finite element simulation presented employs a Saint Venant-Kirchoff material property for the annulus and sinus when it has been shown that the tissues exhibit non-linear deformation in response to stress [50]. The leaflets and root structures were assigned separate but uniformly distributed thicknesses, when reality indicates that thickness varies greatly with region [9-10]. The cross section of the structures was assumed to be homogeneous, but histological examination of the tissue reveals it is truly heterogeneous. This is of primary importance when analyzing the bending stress in the valve, because the bending stiffness in the actual valve tissue includes leaflet structures such as the spongiosa, which introduces a complex bending response. The material model for BAV and TAV is the same in this analysis. However, BAV presence is known to have an impact on valvular

tissue development, and therefore it is reasonable to assume BAV will possess different material parameters [6].

The physiological time-varying pressure load applied to the valve structures has been shown to introduce closing geometry and stress patterns in mitral valve models when compared to that of an FSI boundary condition, because when a fluid boundary condition is employed the pressure distribution is non-uniform near the center of the valve axis [51]. The open orifice of TAV1 being 225 mm^2 is closer to the patient image of the same valve in mid-systole with an open orifice of 277 mm^2. This orifice size maybe misleading because it depends on the perspective. Thus, a qualitative analysis was done comparing the motion of the imaged valve to the FE predicted. The assumptions of uniform thickness may be the cause of reduced leaflet motion. Grande et al. have reported that the thickness of the valve in the belly towards the nodulus of Aranti (center of free margin) can vary from 0.18 mm to 2.06 mm [9]. The assumption of uniform thickness carries over to the BAV model because there is little information regarding BAV-specific thickness data. Physiologically there is going to be a gradient blending one surface to another, but accurately capturing this detail may not be possible at this time. A consequence of this assumption may be responsible for the undulations near the attachment edge, but little data is accessible to verify this effect.

6.3 Future Work

The geometries were generated with a future "mesh free" or NURBS-based solid simulation. While still in development, there has been much evidence to support the usefulness of the NURBS modeling [3-4]. Currently there is work in developing an in-house FSI algorithm that utilizes the NURBS-based solid solver. Before the current models are ready for a

NURBS-based solid simulation two objectives need to be complete. The first is to establish consistent continuity between patches, and the second is to establish the method that the code uses to read in these values. Thubrikar et al. found the median age of surgery for 96 diseased valves (48% bicuspid) was 45–80 years, with an average of 56 [29, 47]. Therefore, it is reasonable to assume that during childhood the aortic valve poses compensatory mechanisms to prevent failure. One such mechanism is physical remodeling of the tissue, including changes in thickness and microstructure. These compensatory mechanisms, in response to congenital abnormalities, may contribute to premature valve failure. In a more patient-based health care framework, anticipation of surgical intervention is key to developing effective treatment strategies.

Future work should focus on the validation of experimental data, which could be improved by utilizing a more accurate approach for boundary extraction from the echo images. Methods of employing a more physiologically realistic thickness to the leaflets will need to be developed so that it can be carried over to a corresponding BAV analysis. With enhanced data corresponding to thickness and valve tissue constituents (TAV and BAV), a more accurate fiber-reinforced model could be developed. Future modeling of soft tissue fibers could be utilized in a more multiscale analysis. Seen in the stress contour plots, there is a region of increased stress. The location of this increased stress coincides with locations known to include raphe. In the future, changes to the material property due to the raphe could be simulated.

REFERENCES

1. Chandran KB, Rittgers SE, Yoganathan AP. Biofluid mechanics : the human circulation. Boca Raton: CRC/Taylor & Francis; 2007.

2. Chandran K. Role of Computational Simulations in Heart Valve Dynamics and Design of Valvular Prostheses. Cardiovascular Engineering and Technology. [10.1007/s13239-010-0002-x].2010;1(1):18-38.

3. Lu J. Isogeometric contact analysis: Geometric basis and formulation for frictionless contact. Computational Methods of Applied Mechanical Engineering. 2010 October 2 200:15.

4. Hughes TJR, Cottrell JA, Bazilevs Y. Isogeometric analysis: CAD, finite elements, NURBS, exact geometry and mesh refinement. Computational Methods of Applied Mechanical Engineering. 2004;194:60.

5. Fedak PW, Verma S, David TE, Leask RL, Weisel RD, Butany J. Clinical and pathophysiological implications of a bicuspid aortic valve. Circulation. 2002 Aug 20;106(8):900-4.

6. Yener N, Oktar GL, Erer D, Yardimci MM, Yener A. Bicuspid aortic valve. Ann Thorac Cardiovasc Surg. 2002 Oct;8(5):264-7.

7. Ward C. Clinical significance of the bicuspid aortic valve. Heart. 2000 Jan;83(1):81-5.

8. Otto CM. Calcification of bicuspid aortic valves. Heart. 2002 Oct;88(4):321-2.

9. Grande JK, Cochran RP, Reinhall PG, Kunzelman KS. Stress variations in the human aortic root and valve: the role of anatomic asymmetry. Annals of Biomedical Engineering. 1997;26:9.

10. Grande JK, Cochran RP, Reinhall PG, Kunzelman KS. Mechanisms of Aortic Valve Incompetence: Finite Element Modeling of Aortic Root Dilatation. The Society of Thoracic Surgeons. 2000 December 21, 1999;69:6.

11. Gnyaneshwar R, Kumar RK, Balakrishnan KR. Dynamic analysis of the aortic valve using a finite element model. Ann Thorac Surg. 2002 Apr;73(4):1122-9.

12. Kim H, Lu J, Sacks MS, Chandran KB. Dynamic simulation of bioprosthetic heart valves using a stress resultant shell model. Ann Biomed Eng. 2008 Feb;36(2):262-75.

13. Kim H, Lu J, Sacks MS, Chandran KB. Dynamic simulation pericardial bioprosthetic heart valve function. J Biomech Eng. 2006 Oct;128(5):717-24.

14. Kim H, Chandran KB, Sacks MS, Lu J. An experimentally derived stress resultant shell model for heart valve dynamic simulations. Ann Biomed Eng. 2007 Jan;35(1):30-44.

15. Conti CA, Votta EV, Corte AD, Viscovo LD, Bancone C, Cotrufo M, et al. Dynamic finite element analysis of the aortic root from MRI-derived parameters. Medical and Engieering Physics. 2009;32:9.

16. Conti CA, Corte AD, Votta EV, Viscovo LD, Bancone C, De Santo LS. Biomechanical implications of the congentical bicuspid aortic valve: a finite element study of aortic root function from in vivo data. Thoracic and Cardiovascular Surgery. 2010;140:6.

17. Chandran KB, Kim SH, Han G. Stress distribution on the cusps of a polyurethane trileaflet heart valve prosthesis in the closed position. J Biomech. 1991;24(6):385-95.

18. Sun W, Abad A, Sacks MS. Simulated bioprosthetic heart valve deformation under quasi-static loading. J Biomech Eng. 2005 Nov;127(6):905-14.

19. Fung YC, Fronek K, Patitucci P. Pseudoelasticity of arteries and the choice of its mathematical expression. Am J Physiol. 1979 Nov;237(5):H620-31.

20. De Hart J, Peters GW, Schreurs PJ, Baaijens FP. A three-dimensional computational analysis of fluid-structure interaction in the aortic valve. J Biomech. 2003 Jan;36(1):103-12.

21. Arcidiacono G, Corvi A, Severi T. Functional analysis of bioprosthetic heart valves. J Biomech. 2005 Jul;38(7):1483-90.

22. Hakuno D, Kimura N, Yoshioka M, Fukuda K. Molecular mechanisms underlying the onset of degenerative aortic valve disease. J Mol Med. 2009 Jan;87(1):17-24.

23. Sacks MS. A Method for Planar Biaxial Mechanical Testing That Includes In-Plane Shear. Journal of Biomechanical Engineering. 1999;121(5):551-5.

24. Billiar KL, Sacks MS. A method to quantify the fiber kinematics of planar tissues under biaxial stretch. Journal of Biomechanics. [doi: DOI: 10.1016/S0021-9290(97)00019-5]. 1997;30(7):753-6.

25. Billiar KL, Sacks MS. Biaxial Mechanical Properties of the Native and Glutaraldehyde-Treated Aortic Valve Cusp: Part II---A Structural Constitutive Model. Journal of Biomechanical Engineering. 2000;122(4):327-35.

26. Billiar KL, Sacks MS. Biaxial Mechanical Properties of the Natural and Glutaraldehyde Treated Aortic Valve Cusp---Part I: Experimental Results. Journal of Biomechanical Engineering. 2000;122(1):23-30.

27. Kim S, Izumi Y, Yano M, Hamaguchi A, Miura K, Yamanaka S, et al. Angiotensin blockade inhibits activation of mitogen-activated protein kinases in rat balloon-injured artery. Circulation. 1998 May 5;97(17):1731-7.

28. Jermihov PN, Jia L, Sacks MS, Gorman RC, Gorman III JH, Chandran KB. Effect of geometry on the leaflet stresses in simulated modesl of congenital bicuspid aortic valves. Cardiovascular Engineering and Technology. 2011;2(1):8.

29. Robicsek F, Thubrikar MJ, Cook JW, Fowler B. The congenitally bicuspid aortic valve: how does it function? Why does it fail? Ann Thorac Surg. 2004 Jan;77(1):177-85.

30. Weinberg EJ, Kaazempur Mofrad MR. A multiscale computational comparison of the bicuspid and tricuspid aortic valves in relation to calcific aortic stenosis. Journal of Biomechanics. [doi: DOI: 10.1016/j.jbiomech.2008.08.006]. 2008;41(16):3482-7.

31. Sievers HH, Schmidtke C. A classification system for the bicuspid aortic valve from 304 surgical specimens. J Thorac Cardiovasc Surg. 2007 May;133(5):1226-33.

32. Subramanian R, Olson LJ, Edwards WD. Surgical pathology of pure aortic stenosis: a study of 374 cases. Mayo Clin Proc. 1984 Oct;59(10):683-90.

33. Sadee AS, Becker AE, Verheul HA, Bouma B, Hoedemaker G. Aortic valve regurgitation and the congenitally bicuspid aortic valve: a clinico-pathological correlation. Br Heart J. 1992 Jun;67(6):439-41.

34. Braverman AC, Güven H, Beardslee MA, Makan M, Kates AM, Moon MR. The Bicuspid Aortic Valve. Current Problems in Cardiology. [doi: DOI: 10.1016/j.cpcardiol.2005.06.002]. 2005;30(9):470-522.

35. Togashi M, Tamura K, Masuda Y, Fukuda Y. Comparative study of calcified changes in aortic valvular diseases. J Nippon Med Sch. 2008 Jun;75(3):138-45.

36. Collins MJ, Butany J, Borger MA, Strauss BH, David TE. Implications of a congenitally abnormal valve: a study of 1025 consecutively excised aortic valves. J Clin Pathol. 2008 April;61(4):530-6.

37. Wakhloo AK, Tio FO, Lieber BB, Schellhammer F, Graf M, Hopkins LN. Self-expanding nitinol stents in canine vertebral arteries: hemodynamics and tissue response. AJNR Am J Neuroradiol. 1995 May;16(5):1043-51.

38. Garcia D. KL. What do you mean by aortic valve area: geometric orifice area, effective orifice area, or Gorilin area? The Journal of Heart Valve Disease. 2006 September 2006;15:8.

39. Zigelman CZ, Edelstein PM. Aortic Valve Stenosis. Anesthesiology Clinics. [doi: DOI: 10.1016/j.anclin.2009.07.012]. 2009;27(3):519-32.

40. Shier D, Butler J, Lewis R. Hole's human anatomy & physiology. Dubuque, IA: McGraw-Hill; 2007; 11th:[xxvii, 1043 p.].

41. Bhatti AM. Fundamental finite element analysis and applications. Hoboken, New Jersey: John Wiley & Sons, Inc.; 2005.

42. Fung YC. Biomechanics: Mechanical Properties of Living Tissues. 2nd ed. New York: Springer-Verlag; 1993.

43. documentation A. v6.8.1. 2010.

44. Cataloglu A, Clark RE, Gould PL. Stress analysis of aortic valve leaflets with smoothed geometrical data. J Biomech. 1977;10(3):153-8.

45. Chuong CJ, Fung YC. On Residual Stresses in Arteries Three-Dimensional Stress Distribution in Arteries. Journal of Biomechanical Engineering.1986;108(2):189-92.

46. Pomerance A. Pathogenesis of aortic stenosis and its relation to age. Br Heart J. 1972 Jun;34(6):569-74.

47. Thubrikar MJ, Aouad J, Nolan SP. Patterns of calcific deposits in operatively excised stenotic or purely regurgitant aortic valves and their relation to mechanical stress. Am J Cardiol.1986 Aug 1;58(3):304-8.

48. Levitt LC, Thubrikar MJ, Nolan SP. Patterns and pathogenesis of calcification in pathologic human aortic valves. Curr Surg. 1984 Jan-Feb;41(1):17-9.

49. Goldbarg SH, Elmariah S, Miller MA, Fuster V. Insights into degenerative aortic valve disease. J Am Coll Cardiol. 2007 Sep 25;50(13):1205-13.

50. Martin C, Pham T, Sun W. Significant differences in the material properties between aged and human porcine aortic tissues. European Journal of Cardio-throacic Surgery. 2010;40:6.51.Lau KD, Diaz V, Scambler P, Burriesci G. Mitral valve dynamics in structural and fluid- structure interaction models. Medical Engineering & Physics. 2010;32:7.

APPENDIX

AORTIC VALVE RECONSTRUCTION PROTOCOL

Section 1

Contact surface construction

Section 2

Leaflet construction

Section 3

Annulus construction

Section 4

Sinus construction

Section 1: Contact Surface Construction

The data provided for the contact area of the leaflets is a single zero-thickness surface. For an FE valve analysis, there must be some initial gap introduced between the leaflets to prevent initial contact numerical problems. For this purpose, each imported contact area is rotated +/- 7 degrees to create surfaces for adjacent leaflets. The rotation is about the "height of commissure" axis to ensure continuity of the root (created later). An example of completed contact surfaces generated as mentioned are shown in Figure 4.

Section 2: Leaflet Construction

The second structure to be constructed should be the leaflets. To accurately capture the leaflet area, it is important to identify the leaflet attachment boundary, or LAB. The LAB is a single curve that bounds the outer edge of the leaflet, the top of the annulus, and the base of the sinus.

Group the generated contact surfaces individually and hide them from view. Import the point cloud data corresponding to each leaflet and make sure to group each leaflet separately for easy manipulation later. Show all of the point cloud data. Locate the single vertex corresponding to the "height of commissure" at each leaflet junction (usually the uppermost vertex of the rotation axis used for contact surface generation) and connect them using b-splines in order to capture the most probable LAB. In this step, use a control point curve to smooth the change of curvature from the vertical contact surface to the near orthogonal leaflet belly. An LAB that has been identified but not smoothed is shown in

Figure A1.

Once smooth LAB b-splines have been identified, remove the vertices that were used to generate them and create new vertices on the LAB so that there exists 18 equally sized sections to each leaflet. Group the vertices and b-spline that defines the LAB. Next, un-hide (show) a point cloud group corresponding to a single leaflet belly and contact surface, including the LAB. Create the free edge of the leaflet by using control-point and interpolated b-splines from the uppermost portion of the annulus and the contact surfaces. Given the approximate height of coaptation of each leaflet, start a b-spline from the third point down from the height of commissure to bound the lower portion of the contact area to the LAB. This step will require a combination of control point and interpolated b-splines to achieve the most realistic interpretation of the actual geometry. In a similar fashion, connect left and right sides of the LAB with interpolated b-splines, utilizing all vertices of the leaflet belly. The result should be 8 horizontal b-splines defining a single leaflet, merged with the LAB. Remove all vertices of the leaflet, less the ones defining the 18 sections of the LAB. Place vertices on the free edge to create 12 equally spaced sections. Do the same for two lines below. The b-spline that begins with the fifth vertex below the height of commissure generates 10 equally spaced sections, for the sixth, 8 sections; seventh, 6 sections; eighth, 4 sections; ninth, 2 sections. Starting at the fifth vertex from the top of the commissure, create a "vertical" b-spline that uses the nearest points in succession to the free edge. Repeat this to generate 12 vertical sections. Next, remove the previously made horizontal b-splines and vertices less the free edge. Create four equally spaced sections on the two outermost vertical b-splines (not removed in the previous step), and then create 5 equally spaced sections on the second outermost b-splines. Continue this to the central b-spline, which should have 9 total sections. Create horizontal b-splines

similar to the free edge, but utilize the vertices made in the vertical b-splines. Repeat this process for all leaflets. For easy future steps, group the LAB curve and vertices. The final product should be similar to the leaflets shown in Figure A2.

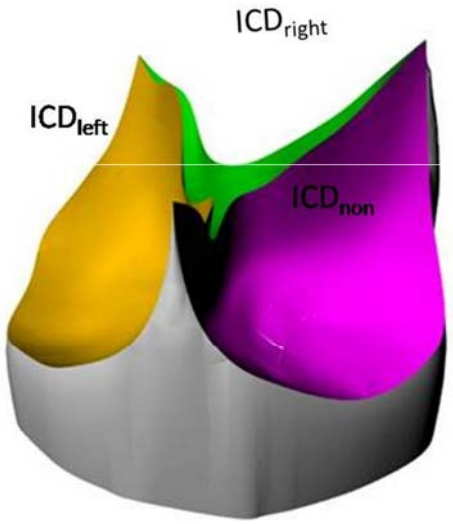

Figure A2. completed annulus and leaflet structure.

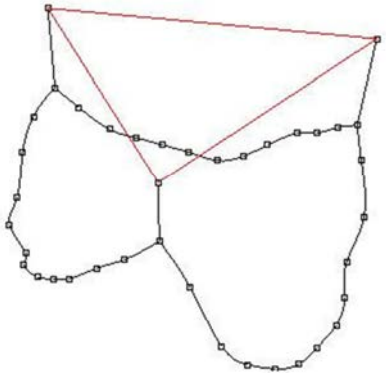

Figure A1. Leaflet attachment boundary identified for TAV. Inter-commissural distances shown in red for visualization purposes.

Section 3: Annulus Construction

Create a circle using the lowest portion of the LAB curves. Create another circle using the uppermost vertices of the leaflet commissures (top of annulus). Create a vertex in the center of each circle created (in-plane). Linearly connecting these should create a "central" axis for the valve. Extend the central axis to 5 mm below the lowest portion of the LAB, and move the lower circle to this point. Generate a surface from the circle that lies 5 mm below the base of the LAB. An example of this operation is shown in Figure A3. Increase the size of the circular area by a factor of two. Using a pull/project tool, select the vertices of the LAB and project them on the circular area generated below. Hide the projection target. Create the lower portion of the annulus using the projected points. Connect the vertices of the LAB to the project points, linearly. If this is a problem of leaflet-annulus intersection, scale the size of the lower annular points (retaining the distribution) to create a base that allows for more leaflet clearance without geometrical intersection. A maximum of 20% increase in lower annular area was needed.

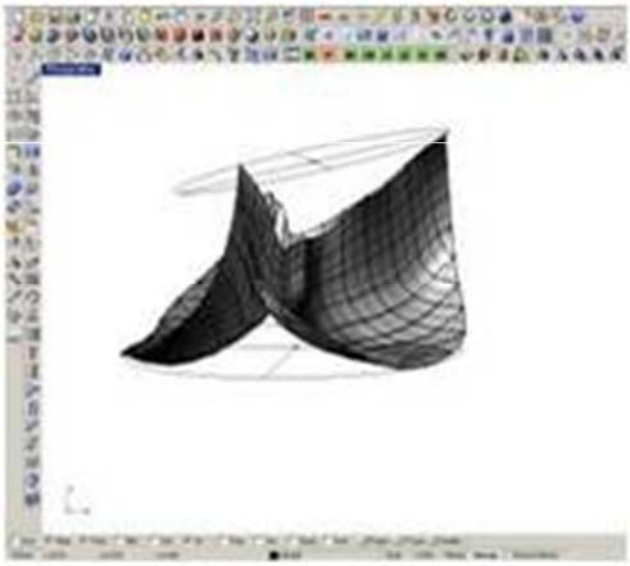

Figure A3. Circular planes generated for annulus and sinus construction.

Section 4: Sinus Construction

Hide all surfaces generated less the central axis, LAB curve, lower circular "target area," and vertices corresponding to the LAB. Import data corresponding to the root. Visualize where the root data intersects the LAB data. Typically they should be in good agreement and overlap. Remove the vertices that are assigned to the root but are near redundant with the LAB vertices. Create vertical b-splines beginning with the lowest vertex of the root (after removing the point closest to the LAB). Move the target area along the central axis so that the area is just above the sinotubular junction region identified in the data. Use the target surface to cut the b-splines that extend past it and project the points that lie below it to create an upper boundary for the root. Remove all vertices less the bounding points of the vertical b-splines made from the patient data. Generate 15 equal sections on each. Horizontally connect the rows of vertices created on the vertical b-splines. Delete the vertical lines and reveal the LAB and associated points. Generate vertical b-splines originating from the LAB to just above the STJ. Generate 4 evenly spaced sections along the b-splines that extend from the top of the height of commissure to the uppermost portion of the sinus. Generate vertices to connect the heights of commissures of each valve using the sinus points. Split the b-splines vertically where the heights of commissures are connected horizontally. Above the split, create 4 sections. Below the split, create sections so that they can be equally connected. Connect the vertices horizontally. The root assembly and process is shown in Figure A4. The final assembly needs to be reoriented to be parallel to the desired plane. Finally, the vertices and b-splines are removed. The model is then exported into an ASCII file format.

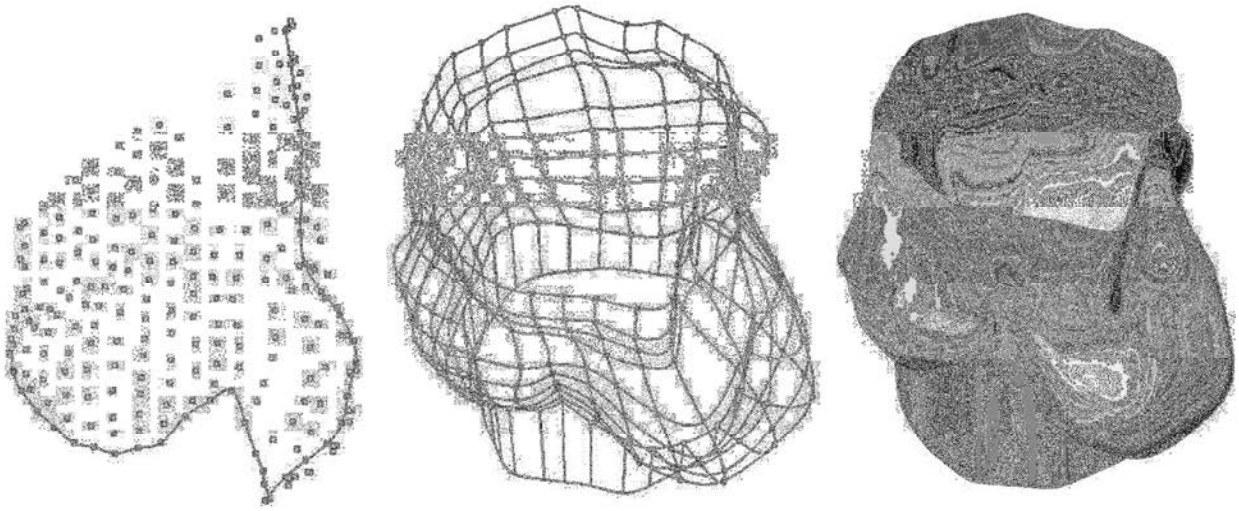

Figure A4. Sinus generation from point cloud data.